Impact of Ge content on the electrochemical performance of Germanium Oxide/Germanium/ reduced graphene (GeO$_2$/Ge/r-GO) hybrid composite anodes for lithium-ion batteries

Christian Randell Arro , Assem Taha Ibrahim Mohamed , Nasr Bensalah [*]

Program of Chemistry, Department of Chemistry and Earth Sciences, College of Arts and Sciences, Qatar University, P.O. Box 2713, Doha, Qatar

ABSTRACT

Hybrid composites between Germanium (Ge) and carbonaceous materials have been extensively studied due to the carbonaceous' component's ability to mitigate the intrinsic problems pertaining to Ge-based anodes. The mitigation of reduced cycling ability and rate capability allows for the unhindered benefit of higher capacities in Ge-carbonaceous composite anodes. Here, the effect of different Ge mass loading on electrochemical performance is studied on a GeO$_2$/Ge/r-GO composite made using controlled microwave radiation of ball-milled Ge and sonicated dispersion of graphene Oxide (GO) as a lithium battery anode. The composite anode at Ge 25% showed greatest cycling retention with 91% after 100 cycles and an average specific capacity of 300 mAh/g (1600 mAh/g Ge). At 75% Ge mass loading the anode suffered with limited cycling retention of 57.5% at the cost of greater specific capacities. The composite at 50% Ge attained advantageous characteristics of both composites with a stable cycling performance of 71.4% after 50 cycles and an average specific capacity of 400 mAh/g (1067 mAh/g Ge, all conducted at a current density of 100 mA/g). A positive linear correlation is revealed for increasing Ge mass loadings and specific capacities in Ge-carbonaceous as anode materials.

1. Introduction

As research looks toward renewable energies such as solar and wind, the means of energy storage grows equally as important. A stimulant into researching energy storage devices, particularly batteries, is the growth of electric vehicles (EVs) and its similar constituents such as battery electric vehicles (BEVs). In 2019 alone, the global stock of EVs reached 7.2–7.5 million units, with around 67% belonging to BEVs alongside a growing trend as the market shares reached 2.6% in 2019 [1, 2]. With the impressive growth of the EV market, the demand for superior batteries with better parameters are becoming more imperative as they may allow EVs to have further travel ranges and longer lifespans which relates to the battery materials' energy density/capacity and cycling stability [1–4]. Prospective new battery materials are now under rigorous critique in determination of whether they are viable for low-cost manufacturing. The mining of elements needed for battery materials as well as their abundance plays an important role in determining the viability of an element as a precursor for battery materials. As such, research into moving the market away from the established cobalt-rich cathode materials and carbon-based anode materials is

becoming a more prevalent approach to solve the EV's demands [1,2]. One approach to meet the demands are attempts on the anode side of lithium-ion batteries (LIBs). The replacement of graphite (with theoretical specific capacity of 379 mAh/g) as an anode for a material with higher capacity is being researched, driven by the EVs demand. Germanium (Ge) primarily presents itself as a good candidate as anode for high-energy density batteries with improved cycling stability. Powered by the alloy/de-alloy phenomenon, Ge and its fellow group IV members exhibit more specific energy capacities and energy densities [3]. Ge is reported to have a theoretical capacity of 1600–1650 mAh/g whilst Silicon (Si) achieves 4200 mAh/g theoretical capacity [5–8]. Ge receives less attention when compared to Si because Ge has a higher cost and lower capacity. However, Ge holds the advantage over Si in certain aspects such as electrical conductivity and lithium diffusivity. Ge has a much greater electrical conductivity than Si at more than 10,000 times because of the small band gap of approximately 0.6 eV and when comparing lithium diffusivity, Ge gains advantage with more than 400 times the amount of Si which makes Ge much suitable for high-power and high-current LIBs [3–8]. Unlike Si, Ge experiences isotropic swelling and a tough behavior whereas Si has anisotropic swelling which

ultimately leads to surface fracture and a fragile behavior [5,6]. A common downfall pertaining to both Ge and Si materials would be the repeated drastic volume expansion and contraction of 370% and 420% respectively that eventually leads to capacity losses because of the pulverization of anode particles, thereby restricting their functionality in further electrochemical reactions resulting in poor cycling performance [4–8].

On the other hand, there is significance to work on germanium-based anodes when compared to graphite and carbon-based compositions. Commercialized graphite-based anodes have shown stable marketability due to their cheap and environmentally friendly (recyclability) properties; they are not without fault [9,10]. Graphite-based anodes suffer from low capacities due to the formation of traditional LiC_6 during the intercalation of lithium into the graphitic structure [9–11]. Furthermore, these anodes suffer from poor rate capabilities due to slow perpendicular lithium-ion intercalation, among other complex reasons [11,12]. Many methods have been evaluation as solutions to improve the property through surface modifications and addition of supporting structures [9,13,14]. Still, a crucial route to improve the low capacities in graphite anodes would be through alloy-type anodes, in specific group IV elements and their oxide derivatives. In such composite scenarios, flexible graphite structures help to sustain the volumetric change of group IV elements whilst the graphite components receive improved capacity help from the group IV components [15,16].

Ge/C nanocomposites have been made, where the carbon framework acts as a preventative measure against the large volume change which consequently mitigates the pulverization of the anode whilst increasing electrical conductivity [17]. Ge/N-doped carbon nanostructure anode studies have also shown drastic improvement as the N-doped carbon framework offered diffusion pathways as well as spaces to accommodate for the large volume changes during lithiation/delithiation [18]. Another study using *in-situ* synthesized Ge/reduced graphene oxide (Ge/r-GO) highlights the structural stability of the r-GO while providing a large contact area with the electrolyte [19]. An effective route to restrict the inherent volumetric change of Ge during lithiation and delithiation would be nano structuring. The implementation of nano-structured Ge architecture has allowed the material to overcome the pulverization difficulties as well as provide further benefits depending on the structure types. Nanowire (NW) Ge have shown, on multiple occasions, the feasibility of this approach by not only bypassing the pulverization of Ge anodes – but also providing improved electrical conductivity throughout the length of the NW, high surface-area contact with the electrolyte and shortened lithium diffusion pathways [20–22]. The compositing of Ge with other frameworks such as self-compositing dual-ion batteries (DIBs) [23], copper [24], tin [21], silicon [25], and polypyrolle [26] have also highlighted repeatedly the improvement of capacity and retention in composites of Ge, making this approach a common practice to improve battery performance. Studies into using reduced graphene oxide have been shown to improve electrochemical performance. Recently, Ge/GeO$_2$/r-GO composite anode material revealed major improvements on the ionic conductivity and charge transfer within the proposed framework [27].

In this work, Germanium Oxide/Germanium/reduced graphene oxide (GeO$_2$/Ge/r-GO) composite anodes, at three different concurrent Ge weight percentages (25%, 50%, 75%), were developed for LIBs using microwave-assisted synthesis to which characterization *via* scanning electron microscopy (SEM), transmission electron microscopy (TEM), x-ray diffraction (XRD) and energy dispersive x-ray analysis (EDX) was conducted. Moreover, electrochemical testing like galvanostatic charge-discharge (GCD) curves and cyclic voltammetry (CV) were established to gauge the electrochemical performance of the material with specific focus on the electrochemical effect at different Ge loading masses. Post-mortem characterization was conducted for the three GeO$_2$/Ge/r-GO weighted anodes at complete lithiation and delithiation junctions to study the morphological and structural changes in the anode which may provide insight into the reactions of the material through additional techniques like X-ray photoelectron spectroscopy (XPS).

2. Materials and methods

2.1. Synthesis of the GeO$_2$/Ge/r-GO Composite

Pure Ge powder was obtained from Fluka AG. The Ge powder underwent 4 h of ball-milling at 400 rpm using MSK-SFM-1 Planetary Ball Mills. The GO component was synthesized using modified Hummers' method [28] from graphite powder as provided by BDH Chemicals Ltd. GeO$_2$/Ge/r-GO composites were then calculated and synthesized at three approximate weight percentages (wt%), 25%, 50% and 75%. The composites are respectively dubbed Ge25, Ge50 and Ge75 and were prepared in sufficient amount and capacity for the following physical-characterization and electrochemical tests. Preparation for GeO$_2$/Ge/r-GO follows through with the suspension of GO in distilled water by sonification for 30–60 min, followed by the addition of the expected amount of ball-milled Ge. The mixture was then placed inside the cavity of a Monowave 300 Anton Paar microwave reactor and was exposed to controlled radiation at a temperature of 160 °C and pressure of 8 Bar for 30 min. Finally, the composite mixture was centrifuged, washed with distilled water, and dried in a vacuum-oven overnight at 80 °C.

2.2. Characterization methods of GeO$_2$/Ge/r-GO Battery Material

A wide array of characterization techniques was applied to the as-synthesized material. Phase-pure confirmation of GeO$_2$/Ge/r-GO and determination of the Ge/GeO$_x$ components were executed using XRD *via* Empyrean PANalytical from the 2θ diffraction angles 10–100° at Cu K$_\alpha$ radiation (λ = 1.540498 Å). The morphology of the GeO$_2$/Ge/r-GO samples was observed using FEI NOVA NANOSEM 450 equipment. Elemental qualitative analysis was conducted using SEM-EDX analyzer, as well as the progressive change of the Ge:O ratio as an indicator for the formation of GeO$_2$ of GeO$_2$/Ge/r-GO composition. Raman spectroscopy was used with (Thermo Scientific™, DXR™ 2 Raman Microscope) for further characterization of the phase structures and molecular interactions. Additionally, thermogravimetric analysis (TGA) was performed using PerkinElmer TGA 4000 to see the differences in thermal stability of the composite in comparison with the Ge precursor, whilst Brunauer–Emmett–Teller (BET) model was applied to show the change in surface area and the size distribution of pores in the GeO$_2$/Ge/r-GO material.

2.3. Slurry preparation, cell fabrication and electrochemical testing

The GeO$_2$/Ge/r-GO composite was slurry-coated using Super P as a carbon source, polyvinylidene fluoride (PVDF) as a binder, and N-methyl pyrrolidinone (NMP) as a solvent at an active material, carbon, and binder ratio of 0.75: 0.15: 0.10. The slurry was casted onto a copper current collector with a doctor blade applicator and dried in a vacuum oven. The loading mass of GeO$_2$/Ge/r-GO composites used was on average 1.5, 3.0 and 4.5 mg/cm^2 for 25, 50 and 75 Ge wt%, respectively. CR 2032 coin-cells, in half-cell configuration, were fabricated within a glovebox chamber (MTI, VGB-6-LD) under Argon gas environment with O$_2$ and H$_2$O levels below 0.1 ppm. 1 M Lithium bis-(tri-fluoromethanesulfonyl) imide (LiTFSI) in EC/DMC/DEC (1:1:1 in volume) carbonate mixture was used as electrolyte, lithium foil as counter electrode, and Celgard® 2500 as separator. CV investigation was carried out using CS350 Potentiostat/Galvanostat (electrochemical workstation) at a voltage range from 0 to 1.5 V *vs.* Li$^+$/Li and scanning rate of 0.01 mV/s up to 5 cycles whilst GCD tests were done using 8 channel battery analyzer (0.005 −1 mA, up to 5 V) - BST8-WA.

2.4. Postmortem analysis

Cells for Ge25, Ge50 and Ge75 were subjected to postmortem analysis at three conditions; electrode-slurry form (ESF), post-discharge (PD) to 0.05 V *vs.* Li$^+$/Li and post-charge (PC) to 1.2 V *vs.* Li$^+$/Li. Reacted anodes were extracted from the cells whilst within the glove-box environment and were washed with propylene carbonate. Pristine and dried lithiated/delithiated GeO$_2$/Ge/r-GO composites at the three wt% were kept in argon filled vials and opened in Argon environment just before analysis by SEM, TEM, XRD and XPS to evaluate the differences between the three samples at the different charge states and to further investigate the changes seen in electrochemical characterization and performance.

3. Results and discussion

3.1. Material characterization

3.1.1. SEM

Scanning electron microscopy (SEM) was opted to study the structural morphology and distributions of the as-prepared GeO$_2$/Ge/r-GO composite materials brought about by the simple production method. The SEM micrographs revealed that the relatively simple material production method produced unique Ge microcube structures, whilst variations in Ge mass loading led to differences in Ge microcube population distributions. The uniqueness of the depicted morphology, for GeO$_2$/Ge as battery material, is seen in Fig. 1 (a-i) of SEM micrographs of GeO$_2$/ Ge/r-GO in different Ge mass loading (25%, 50% and 75%) at uniform magnifications. Contrary to a variety of anode material investigations using Ge, the formation of GeO$_2$/Ge microcubes at this specification using relatively simple production methods and materials is somewhat rare but still present. This is seen with Ge nanoparticles encapsulated in carbon nano-boxes *via* core-shell designs [29]. The r-GO network was well connected to the GeO$_2$/Ge microparticles (Fig. 1.b and 1.c), enabling good electronic conduction for the composite material. The SEM images of ball milled Ge powder before it was mixed with GO, given in Fig. S.1, confirmed that the agglomerated Ge particles were crystalized in cubic system after the microwave reaction. SEM images revealed an important effect of Ge mass loading on the morphology and the structure of GeO$_2$/Ge/r-GO composite. The SEM micrographs of Ge75, as shown in Fig. 1.a, b, and c, showed a visible presence of cubic microparticles of GeO$_2$/Ge wrapped with r-GO nanosheets. The average cubic edge was in the range 0.8–1.2 μm (Fig. 1.a). Similar morphology of GeO$_2$/Ge microcubes was observed for Ge50, as shown in Fig. 1.d, e, and f. However, less population distribution of GeO$_2$/Ge microparticles compared to the Ge75 SEM micrographs due to lower Ge mass loading. The SEM micrographs for the Ge25 composite showed different morphology and structure from the Ge50 and Ge75 counterparts. The SEM micrographs in Fig. 1.g, h, and i demonstrated the absence of cubic particles with lower Ge mass loading. This examined behavior is not commonly investigated within other GeO$_2$/Ge composite anode studies.
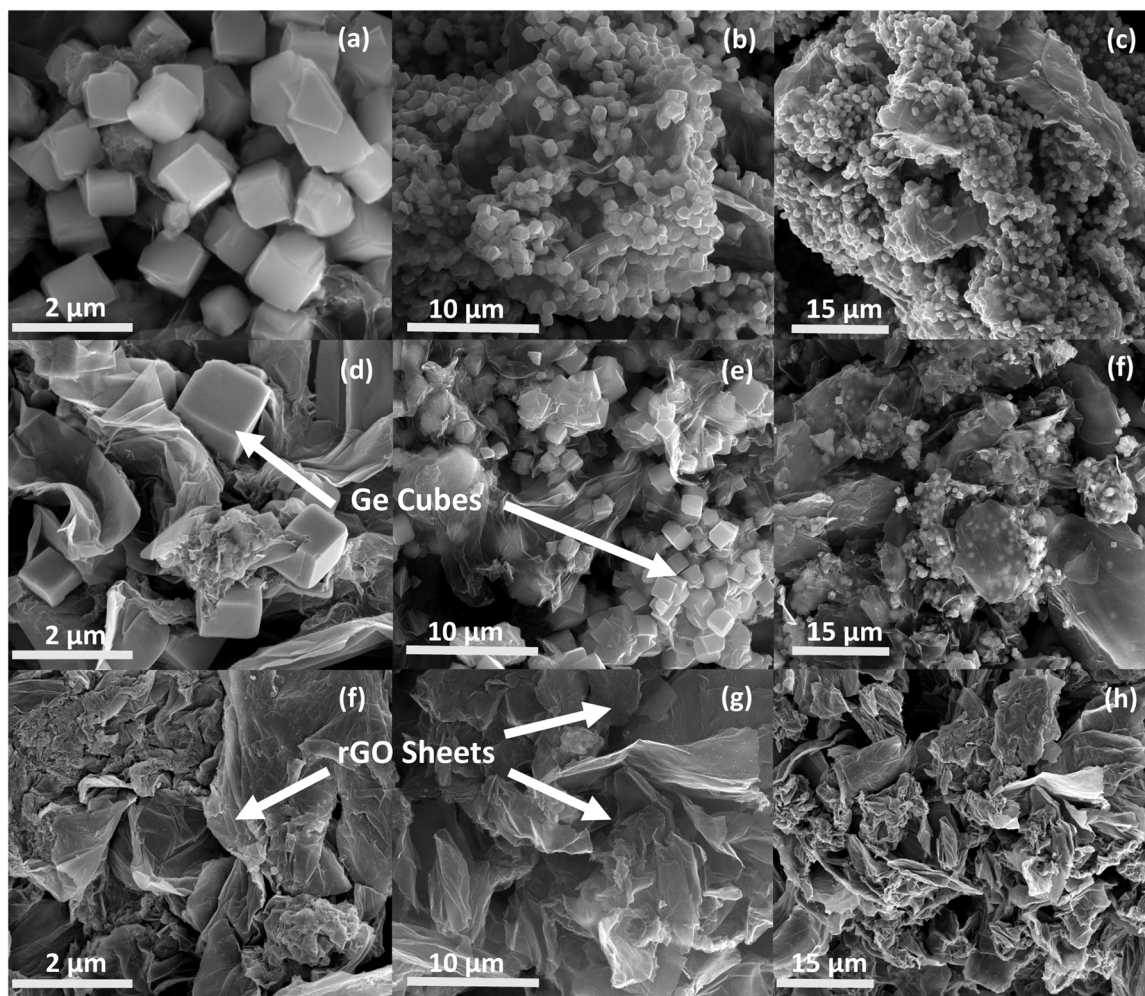

Fig. 1. SEM images at different magnifications of: (a-c) GeO$_2$/Ge75/rGO, (d-f) GeO$_2$/Ge50/rGO, and (g-i) GeO$_2$/Ge25/r-GO composites prepared by solvent-assisted microwave method highlighting the Ge cubes and rGO sheet structures.

3.1.2. EDX

The in-tandem use of EDX was implemented to produce a quantitative analysis to reinforce the SEM micrograph findings. Moreover, EDX not only supports the SEM micrographs, but also provides information on the composition of the materials (see Fig. S.2). After the microwave synthesis, the Ge weight percent were 8.21%, 37.97%, and 62.61% for Ge25, Ge50, and Ge75, respectively. The remarkable decrease in Ge content after the microwave synthesis indicates the involvement of Ge element in the formation of $GeO_2/Ge/r$-GO composite materials. The C weight percent estimates were at 76.91%, 44.09%, and 18.5% for Ge25, Ge50, and Ge75, respectively. On the other hand, the O weight percent was less affected by Ge mass loading (14.88%, 17.94%, 18.89% for Ge25, Ge50, and Ge75, respectively). A closer look on the EDX data, the mole ratio between Ge and O elements shows an interesting observation: as the amount of Ge added increased, the Ge:O mole ratio drops from an average of 1:1 for Ge25 and shifts closer to 1:2 for Ge50 and Ge75. This behavior can be linked to the formation of GeO_2. The increase of Ge:O molar ratio above 1:2 indicates that Ge was partially oxidized to GeO_2 for initial Ge mass loading $\geq$ 50%. This implies that Ge plays a crucial role in the microwave synthesis of $GeO_2/Ge/r$-GO composite material. Evidently, Ge participates in the reduction of GO with formation of GeO_2 and r-GO during microwave irradiation, according to reaction (1):

$$Ge(s) + GO \xrightarrow{microwave \quad radiation} GeO_2(s) + r - GO \qquad (1)$$
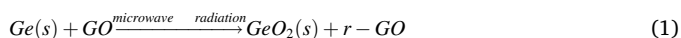
This can be explained by the high microwave absorption of Ge particles (high density of holes in Ge crystalline structure) inducing the transfer of electrons to GO and being oxidized [30]. The remarkable differences in the morphology and structure indicates that the microwave synthesis of $GeO_2/Ge/r$-GO composite material depends largely on the initial Ge mass loading. The reduction of GO by solvent assisted microwave method in presence of Ge to prepare $GeO_2/Ge/r$-GO composites has not been reported in literature based on our knowledge. The microwave method described in this work enabled the synthesis of r-GO-wrapped and GeO_2-coated Ge microparticles with unique morphology and structure. It is noted that very recently Koo and Paek [27] reported the synthesis of $Ge/GeO_2/r$-GO composite using solid-state microwave method. The reported $Ge/GeO_2/r$-GO composite has different morphology and structure than the as-prepared GeO_2-Ge/r-GO composite material reported herein.

3.1.3. TEM

High resolution transmission electron microscopy (HRTEM) provided a different perspective over the $GeO_2/Ge/r$-GO composites, but further supports morphology and structural information as previously seen on SEM micrographs. Fig. 2.**a and b** displayed the cubic shape of GeO_2/Ge microcubes with sizes between 0.8 and 1.2 μm, similar to the SEM results. The r-GO nanosheets framework wrapping GeO_2/Ge particles are clearly depicted in Fig. 2.d to 2.f. Moreover, selected area electron diffraction (SAED) pattern of Fig. 2.g confirmed the crystalline structure of GeO_2/Ge and the SAED spots coincide with the diffraction pattern of (113) and (224) planes of cubic Ge crystalline structure. The D-spacing estimated from the lattice fringes given in Fig. 2.h (0.326 nm) corresponds to (111) planes of cubic crystalline Ge [31].

3.1.4. XRD

To confirm the crystalline nature of Ge within the $GeO_2/Ge/r$-GO composites, XRD was conducted on a sample of Ge50 as seen in Fig. 3. Phase confirmation was attained for the presence of cubic Ge (JCPDS: 98–004–4841), hexagonal GeO_2 (JCPDS: 98–005–3870), and tetragonal GeO_2 (JCPDS: 98–063–7460) with no underlying impurities detected. Hexagonal GeO_2 is the predominant crystalline structure of GeO_2 present in the composite sample of Ge50. The essential peaks for the Ge component were found using Braggs' law, specifically at lattice index (111), (220), (311), and (400), while the indexing of multiple peaks for hexagonal GeO_2 and tetragonal GeO_2 were complimenting with JCPDS databases and supporting XRD reports of GeO_2 [32–34]. The lattice indexing of the crystalline Ge coincided with TEM fringing results. GO used in preparation of the as-synthesized material was analyzed producing an XRD spectra highlighting the presence of the GO and r-GO peaks at 10° and 20.3°, respectively. The XRD spectrum of the as-synthesized showed the absence of GO characteristic peak at 10° with no formation of other GeO_x components, further supporting GeO_2 being the only GeO_x component. It is possible that the lack of r-GO and carbon component peaks may be absent as a result of masking by the high intensity hexagonal GeO_2 (101) and Ge (111) peaks [35]. The synthetic procedure of the material provides insight about the drastic intensity difference between the hexagonal GeO_2 (101) and Ge (111) in which the microwave reaction provided an environment that oxidizes Ge and reduces GO with formation of GeO_2 and r-GO. The cubic Ge microparticles were coated with GeO_2 thin layer and wrapped with r-GO nanosheets. The thickness of GeO_2 layer coating Ge crystals depend on the initial Ge
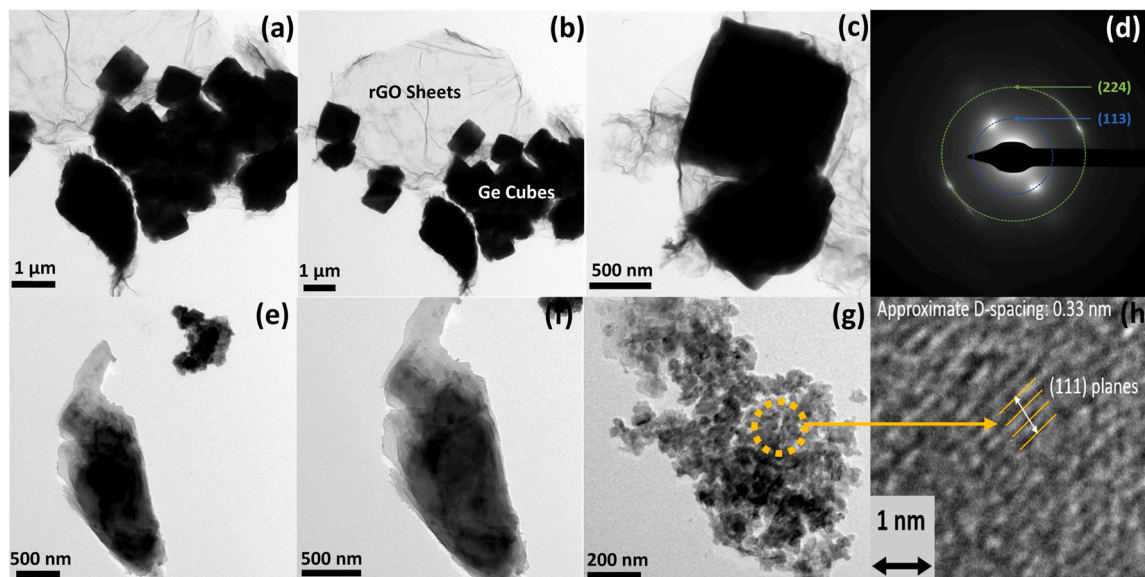

Fig. 2. (a-f) HRTEM images at different magnifications, (g) SAED pattern, and (h) lattice fringes of $GeO_2/Ge50/r$-GO composite prepared by solvent-assisted microwave synthesis method.
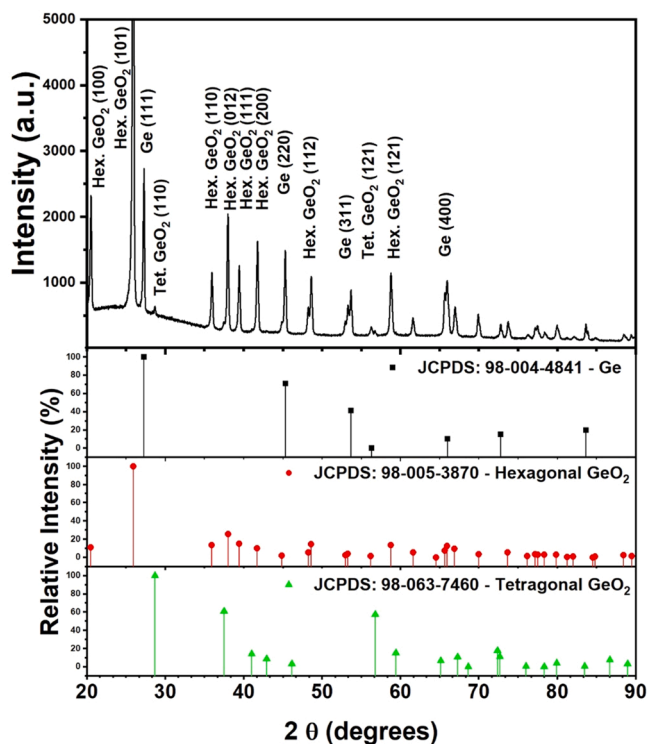
Fig. 3. Indexed XRD spectrum from $2\theta = 10° - 90°$ of the GeO$_2$/Ge50/r-GO composite with cubic Ge and hexagonal and tetragonal GeO$_2$ references.

mass loading.

3.1.5. Raman spectroscopy

To overcome the possible masking of GO and r-GO within the XRD analysis and further confirm the formation of GeO$_2$ and Ge, Raman spectroscopy was used as seen in Fig. 4 Extensive information was obtained by Raman spectroscopy starting from the formation of r-GO, which was confirmed in the sharp Raman peaks located at around 1350 cm^{-1} and 1600 cm^{-1}, designated as D-band and G-band, respectively. These bands correspond to the structural defects within the graphene sheets for the first order Raman D-band peak, whilst the G-band refers to the in-plane vibrations of pristine graphene sheets [36–38]. The ratio between the intensities of the D-band (I$_D$) and G-band (I$_G$) (I$_D$/I$_G$) were calculated to be 0.89 and 1.22, for GO and Ge50 composite. The increase of I$_D$/I$_G$ can be linked to the structural defects pertaining to the disruption of sp^2-carbon bonds [27], proving the reduction of GO sheets
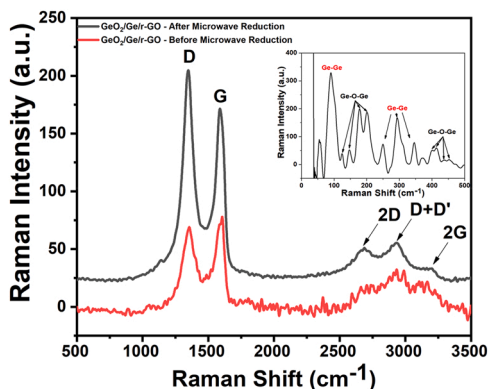
into r-GO. The (I$_D$/I$_G$) ratio > 1 suggests that the synthesized material contains more imperfections because of sp^2-carbon disruptions compared to pristine GO. Furthermore, 2D, D+D′, and 2 G bands located between 2500 cm^{-1} and 3200 cm^{-1} (reported for r-GO samples) [39] confirmed the presence of r-GO in the composite material. The presence of 2D, D + G, and 2 G bands is attributed to the electronic structure perturbations of sp^2 carbons, especially the D + G that is a combination scattering band activated in the presence of structural defects [40–42]. It also indicates the high degree of GO reduction and the excellent electronic conductivity of the reduced GO framework. Raman spectra at higher magnification x50 enables to observe the Raman shifts in the region $0 – 500$ cm^{-1}. The Raman peaks located at 93 cm^{-1}, 254 cm^{-1}, 298 cm^{-1}, 348 cm^{-1} were attributed to Ge-Ge bond [43]. The Raman shifts at 127 cm^{-1}, 150 cm^{-1}, 181 cm^{-1}, 205 cm^{-1}, 405 cm^{-1}, 418 cm^{-1}, 442 cm^{-1}, and 457 cm^{-1} were attributed to Ge-O-Ge in hexagonal and tetragonal GeO$_2$ crystalline structures [44]. This result confirmed the XRD data suggesting the coating of Ge with GeO$_2$ layer.

3.1.6. TGA and BET analysis

TGA was conducted on the Ge50 composite and the Ge metal precursor, as seen in (Fig. S.3), to understand the material behavior and stability at extreme temperatures up to 950 °C. The TGA plot of Ge50 showed a small and steady weight loss which can be seen starting well below 200 °C and could be attributed to the loss of moisture from the composite sample [27]. After 200 °C, even greater weight loss is experienced which could be the result of decomposition of the reduced graphene oxide material [27]. After 700 °C, the plot depicts a weight gain within the material. This corresponds to TGA studies on the Ge metal, which demonstrates weight gain after 600 °C from the oxidation of Ge to GeO and further GeO$_x$ [7]. Unlike complex materials which have three or more variables of mass change, the Ge50 composite only exhibits three mass changes: moisture loss, decomposition of the reduced graphene oxide and oxidation of the Ge into GeO$_x$ under non-inert conditions. As such, based on the TGA analysis we deduced the carbon content to be 49.6% which is quite like the EDX values of 44.09%. Moreover, applied BET (see Fig. S.4) showed transformative results in surface area between the r-GO precursor and the Ge50 sample from 405.9 m^2/g to 90.64 m^2/g, respectively, whilst Ge metal had a small value of 1.37 m^2/g. The significant improvement of greater surface area provided by the r-GO framework on the GeO$_2$/Ge component allows for better facilitation of electrolyte ion movement [45]. The composite also revealed porous properties with average pore sizes of 5.43 and 2.37 nm for BJH absorption and desorption radii, respectively. This property facilitates the diffusion of Li$^+$ ions across the composite structure, thereby providing better electrochemical performance [27].

3.2. Electrochemical characterization

3.2.1. Cyclic voltammetry

To extensively study the lithiation and delithiation mechanisms of the GeO$_2$/Ge/r-GO anode composites across the different Ge mass loading, CV was performed within a 0–1.5 V vs. Li$^+$/Li voltage range at a 0.01 mV/s scan rate. Scans started with the lithiation of the anode material followed by electrochemical oxidation (delithiation) of lithiated materials as seen in the Fig. 5.a comparative plots. The first observation deduced from the comparative CV plots was that the CV profile of Ge25 is significantly different as compared to the CV profiles of Ge50 and Ge75. Ge25 inclined more towards the outline of CV profiles for carbon-based anodes, with the additional Ge peaks [46,47]. A closer examination of the CV of Ge25 shows that in the first reduction scan, two peaks, one sharp and one broad, are present at 0.525 and 0.15 V vs. Li$^+$/Li, respectively (see Fig. 5.b). At the first oxidation scan, four peaks located at 0.08–0.1, 0.37, 0.52, and 1.2 V vs. Li/Li$^+$ appeared in the CV of Ge25. Although the oxidation peak located at 0.08 – 0.1 V vs. Li$^+$/Li had the greatest oxidation peak intensity in the CV of Ge25, it remarkably decreased in intensity compared to the other oxidation peaks in the

Fig. 4. Raman Spectroscopy of Ge50/GeO$_2$/r-GO at (a) 0 cm^{-1} – 3500 cm^{-1} for the r-GO component at 10x magnification comparing before and after microwave reduction (red and black, respectively) and (b) inset figure of 0 cm^{-1} to 1000 cm^{-1} for the Ge/GeO$_2$ component at 50x magnification.
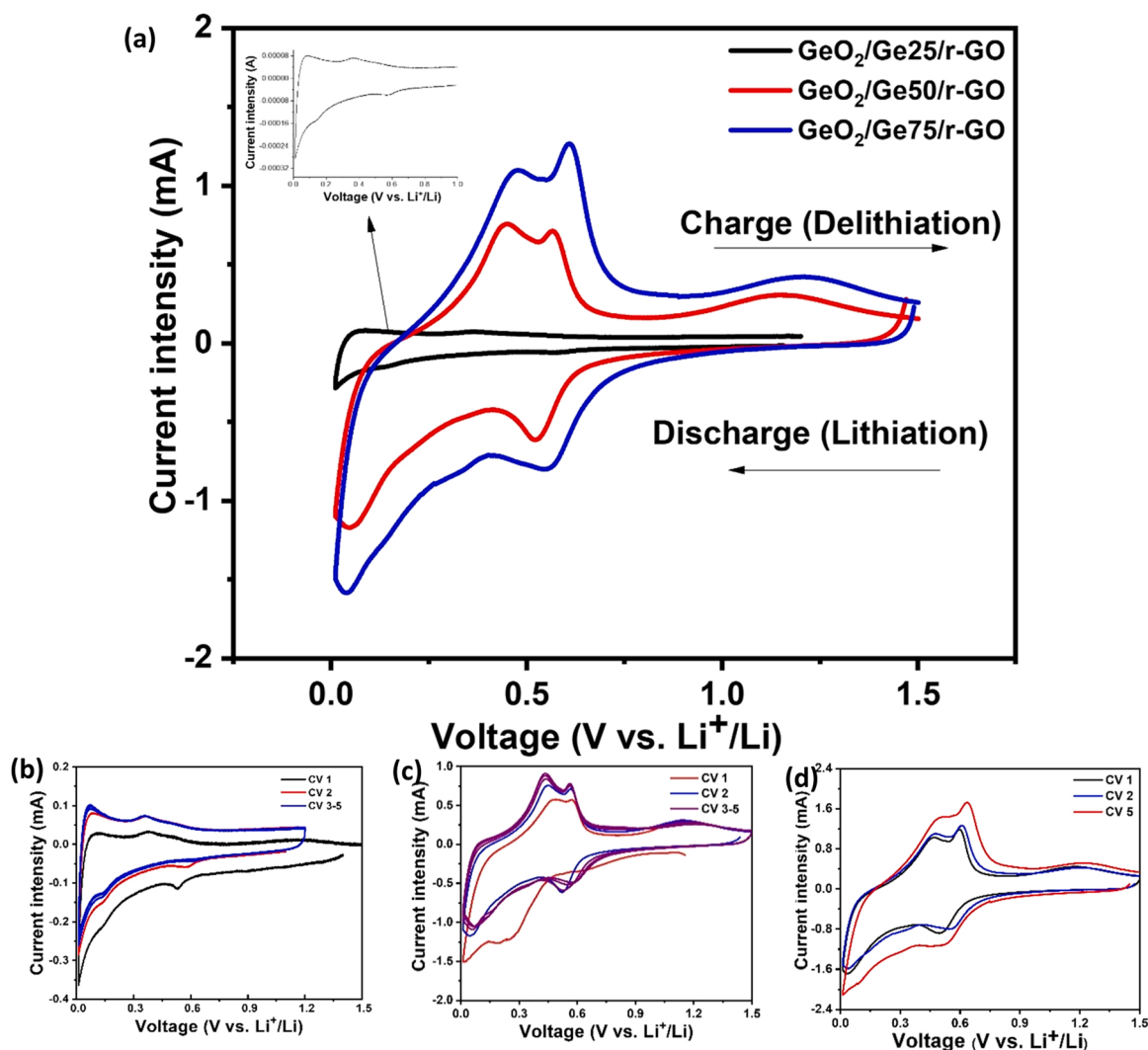
Fig. 5. (a) Comparative CV plot at scan rate of 0.01 mV/s with different Ge mass loading of the three composites GeO$_2$/Ge25/r-GO (black), GeO$_2$/Ge50/r-GO (red) and GeO$_2$/Ge75/r-GO (blue) conducted firstly by discharge to 0.05 V *vs.* Li$^+$/Li followed by charge to 1.5 V *vs.* Li$^+$/Li. Individual CV voltammograms upto 5 cycles from discharge to 0.05 *vs.* Li$^+$/Li followed by charge to 1.2 *vs.* Li$^+$/Li at (b) GeO$_2$/Ge25/r-GO, (c) GeO$_2$/Ge50/r-GO and (d) GeO$_2$/Ge75/r-GO.

CVs of Ge50 and Ge75. This is a characteristic oxidation peak that generally appeared in the CVs of several carbon materials [48–53]. It can be attributed to the deintercalation of Li$^+$ ions between the sheets of r-GO and the carbon additives in the composition of the electrode materials in the case of GeO$_2$/Ge/r-GO composites. It appears that the deintercalation of Li$^+$ ions between the r-GO nanosheets is the main mechanism of Li$^+$ removal in Ge25 composite. The reduction peak at 0.15 V *vs.* Li$^+$/Li can be paired with the first oxidation peak corresponding to reversible intercalation/deintercalation of Li$^+$ ions into/-from r-GO nanosheets in Ge25. The other common oxidation and reduction peaks for the first CVs of GeO$_2$/Ge/r-GO composites can be attributed to alloying/dealloying of Ge and GeO$_2$ and will be discussed in more details with the Ge50 and Ge75 composites. An increase in the intensity of the first oxidation peak and a decrease in the intensities of the reduction peaks were observed in the second CV of Ge25 composite as shown in Fig. 5.b. No apparent changes were detected after the third CV of Ge25 composite indicating the reproducibility and reversibility of the oxidation and reduction processes. A more important phenomenon was observed in relation with the reduction peak located at 0.525 V *vs.* Li$^+$/Li that disappeared after the second CV, indicating that it corresponds to an irreversible process. This phenomenon was reported previously in literature for different anode materials and it was attributed to the formation of SEI thin film on the surface of the anode [54].

As previously mentioned, the CV profile for the Ge25 composite had significant difference as opposed to the composites of Ge50 & Ge75. Further analysis of the CV profile for Ge50 highlighted these differences further (see Fig. 5.c.). In the first reduction scan from 1.5 V to 0.05 V *vs.* Li$^+$/Li, a total of four reduction peaks were detected at 0.66 V, 0.26 V, 0.18 V and a sharp peak at 0.02 V *vs.* Li$^+$/Li. The initial oxidation scan revealed four oxidation peak formations at 0.1 V, 0.47 V, 0.57 V and 1.14 V *vs.* Li$^+$/Li. Unlike the CV profile of the Ge25 composite, there is a significant change in the oxidation peak located at 0.1 V *vs.* Li$^+$/Li in the Ge50 composite CV profile. This oxidation peak, previously attributed as the deintercalation mechanism of Li$^+$ ions between r-GO nanosheets, is seen with a significantly decreased intensity (see Fig. 5.c). Referring to the composition of the as-synthesized composites and the previously cited literature, the change in the oxidation 0.1 V *vs.* Li$^+$/Li peak intensity can be related to the decreased r-GO component ratio within the Ge25 composite as opposed to higher r-GO component ratio in the Ge50 composite. Moreover, this could indicate a decreased contribution of the Li$^+$ ion deintercalation mechanism within the whole delithiation process, discussed further later. More noticeably, the increased development of two adjacent oxidation peaks at 0.47 V and 0.57 V *vs.* Li$^+$/Li are more dominant in the CV profiles of the Ge50 composite as opposed to the Ge25 composite. It is reported in literature that the pair of oxidation peaks represents the delithiation, specifically the de-alloying

mechanism, of Ge with Li [55,56]. It can be noticed that the adjacent oxidation peaks at 0.47 V and 0.57 V *vs.* Li^+/Li have much greater intensity than the 0.1 V *vs.* Li^+/Li oxidation peak. This can indicate a shift in the dominant delithiation mechanism from Li^+ ion deintercalation of r-GO to more Li-Ge de-alloying. This is further supported in the later CV profiles of the Ge75 composite. Of the two adjacent peaks, the left-most-adjacent peak at 0.47 V *vs.* Li^+/Li had the greatest intensity within the CV profile of the Ge50 composite, whilst in the CV profile of the Ge75 composite the corresponding peak at 0.48 V *vs.* Li^+/Li did not have the greatest intensity, but was instead seen at the right-most-adjacent peak at 0.6 V *vs.* Li^+/Li as seen in Fig. 5.d and in the comparative CV plots of Fig. 5.a. The significance of the intensity shifting can be related back to the proposed preparation and composition of the GeO_2/Ge/r-GO composites. It can be correlated that with equal ratios of Ge:GO at 50:50 (Ge50 composites), the formation of GeO_2 surface film over the Ge microcubes is much greater than that at ratios of Ge:GO at 75:25 (Ge75 composites). The limitations created by the smaller GO component limits the formation of GeO_2 surface films, resulting in different intensities of the adjacent oxidation peaks. Under the premise of the previous explanation, we therefore assigned the left-most-adjacent oxidation peak and the right-most-adjacent oxidation peak for the delithiation of GeO_2 and Ge, respectively. It should also be noted, that in the CV profile of the Ge50 composites, the difference of intensity between the adjacent oxidation peaks is not overwhelming. This suggests that the formation of GeO_2 did not overwhelm the amount of Ge present within the Ge50 composite. Another interesting development that can be seen in the CV profile of the Ge50 composite would be the broad oxidation peak centered at 1.15 V *vs.* Li^+/Li, which can also be seen at other CV profiles of the three wt% samples. This oxidation peak has been reported to be an indicator for the possibility of encapsulated Ge in the r-GO nanosheets undergoing oxidation to GeO_2 [45,57]. The implications of this phenomena can be seen in the CV profile of Ge75 composites. The limited formation of the GeO_2 surface films, due to decreased GO component, resulted in larger proportions of Ge in the composite that can undergo this oxidative process. This reflects on the oxidation peaks for CV profiles of the Ge50 composite and Ge75 composite at 1.15 V and 1.2 V *vs.* Li^+/Li, respectively. There is a greater intensity of the corresponding broad oxidation peak in the CV profile of the Ge75 composite at 1.2 V *vs.* Li^+/Li as opposed to the CV profile of Ge50 composite as seen in Fig. 5.a.

Regarding the reduction peaks seen in the CV profile of the Ge50 composites, the first reduction scan that four peaks form at 0.66 V, 0.26 V, 0.18 V and a sharp peak at 0.02 V *vs.* Li^+/Li. The first reduction scan can be assigned as an irreversible process, due to the different shape it presents as opposed to later cycles of the reduction scan. In particular, the reduction peak at 0.66 V *vs.* Li^+/Li only appears in the first cycle. This irreversible occurrence, in addition to the location of the peak, can be related to the SEI formation process, the decomposition of the GeO_2 and initial stages of Li^+-Ge alloying process which is normally found from 0.5 V to 1.0 V *vs.* Li^+/Li [55,57–59]. The influence of this peak can be seen in the other reduction peaks of the same cycle at 0.26 V, 0.18 V and 0.02 V *vs.* Li^+/Li. These reduction peaks, because of the undergoing SEI formation, appear at different intensities compared to their corresponding reduction peaks in later cycles. It has been reported that the alloying of Ge with Li occurs within the reduction region of 0.5–0.1 V *vs.* Li^+/Li [55,57,58]. Therefore, the reduction peaks at 0.26 V and 0.18 V *vs.* Li^+/Li are assigned to the lithiation of Ge with Li whilst the remaining reduction peaks can be assigned to the lithiation of GeO_2. The lack of designation for the reduction peak of the intercalation of Li^+ into the r-GO was credited on the basis that at higher Ge lower r-GO ratios the mechanism of intercalation is overcome and masked by the alloying/de-alloying of Ge with Li. This causal effect is predominant in the CV profiles of Ge50 and Ge75 composites. In the subsequent reduction scans of the CV profile for Ge50, there are very noticeable changes in the reduction peak development. Firstly, the 0.66 V *vs.* Li^+/Li reduction peak disappears because of the formation of a stable SEI layer.

Following this, is the appearance of sharp reduction peak found at 0.52 V *vs.* Li^+/Li, which gradually shifts gently towards higher voltage potential upon further cycling as seen in Fig. 5.c. The subsequent reduction scans reveal two reduction peaks found at 0.34 V and 0.05 V *vs.* Li^+/Li at much weaker intensity but are partially imposed. The partially superimposed characteristic exhibited by the reduction peaks found at 0.52 V, 0.34 V and 0.05 V *vs.* Li^+/Li suggests their participation in the lithiation process of the Ge50 composites as well as their reversibility. As for the oxidation scans, subsequent cycles reveal the same four oxidation peaks at similar voltages – but at noticeably increased intensity. This progressive pattern is also seen at a stronger degree in the CV profile of Ge75 and to a weaker, negligible, degree in Ge25. As seen in Fig. 5.a, the increased in Ge wt%. of the GeO_2/Ge/r-GO composites result in greater current intensities for both the oxidation and reduction scans. The significance of this increasing progression relates the improved kinetics and reversibility of the processes pertaining to the alloying and de-alloying mechanisms.

Like the CV profile of the Ge50 composite, the CV profile of the Ge75 composite consists of similar features. The reduction scan revealed three peaks at 0.55 V, 0.31 V and 0.11 V *vs.* Li^+/Li, whilst the oxidation scan showed four peaks at 0.15 V, 0.46 V, 0.6 V and 1.2 V *vs.* Li^+/Li (see Fig. 5.d). As previously mentioned, is the decreasing oxidation peak assigned to deintercalation of Li^+ ions from the r-GO nano sheets. This is seen and previously explained with the decreasing intensity progressing towards higher Ge and lower carbon ratios. The two adjacent oxidation peaks assigned to the alloying of Ge with Li, with the right most adjacent Ge oxidation peak at 0.6 V *vs.* Li^+/Li having the greater intensity than the left most adjacent GeO_2 oxidation peak at 0.46 V *vs.* Li^+/Li. The 1.2 V *vs.* Li^+/Li peak still corresponds to the oxidation of encapsulated Ge to GeO_2 as previously assigned to in the CV profiles of Ge25 and Ge50 composites. For the reduction scan however, there is no clear designation for the irreversible process of SEI formation, which was previously seen in the CV profiles of Ge25 and Ge50 composites within the voltage range of 0.5–1.0 V *vs.* Li^+/Li. This occurrence has been seen in certain literature in which there is the lack of SEI formation and decomposition of GeO_2 surface films [45,60]. This results in less lithium consumption as part of the irreversible process on the side reactions [45,60]. The lack of SEI formation can be reflected on the overall shape of the CV profile in subsequent cycles. As seen in Fig. 5.d, there is a general shape that is maintained in the reduction and oxidation scans. The lack of SEI reduction peak is produced reduction peaks at 0.55 V and 0.31 V *vs.* Li^+/Li which can be attributed to the alloying formation of Li_xGe. Interestingly, as seen with the CV profiles of Ge50, subsequent CV cycles in the profile for Ge75 reveals even greater intensity progression in both the reduction and oxidation scans. This characteristic once again indicates improved kinetics during lithiation and delithiation of the GeO_2/Ge/r-GO composite.

3.3. Electrochemical performance – GCD

After determination and investigation of the lithiation and delithiation mechanisms of the composite by CV, GCD tests were conducted in the voltage range between 0.05 V and 1.5 V *vs.* Li^+/Li. GCD tests were conducted in the voltage range between 0.05 V and 1.5 V *vs.* Li^+/Li. The current densities and the specific capacities were calculated based on the total mass of the anodes including GeO_2/Ge/r-GO composite, conductive carbon additive and binder (75/15/10 mass percentage, respectively). The voltage profiles of Fig. 6 were plotted at a current density of 100 mA/g for Ge25, Ge50 and Ge75. As opposed to the GCD profiles for Ge50 and Ge75 composite, the GCD profile of the Ge25 composite appeared much different. The GCD profiles of the Ge50 and Ge75 composites displayed charge and discharge plateaus whilst the GCD profile of Ge25 composite showed a smooth curvature and displayed no plateau regions during the charge and discharge stages. The latter GCD profile has been reported with carbonaceous materials anodes and attributed to the intercalation/deintercalation of Li ions during
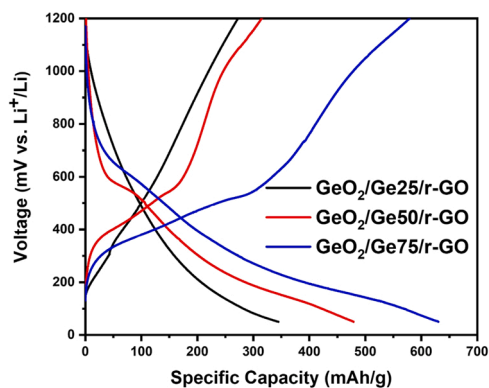
Fig. 6. Effects of Ge Loading from wt% 25, 50 and 75 on the GCD Specific Charge-Discharge Capacities from the first cycle.

discharge/charge cycles [61–64]. These results confirmed the distinct electrochemical behavior observed in CV profile of Ge25 anode compared to the other anodes with higher Ge content. In the comparative GCD plots between the three wt% of Ge (Fig. 6), Ge50 and Ge75 anodes exhibited large discharge plateaus extending in the regions 0.60 – 0.40 V and 0.20 – 0.05 V *vs.* Li+ /Li, corresponding to the lithiation of Ge and GeO_2. Large charge plateaus were observed in the region 0.3 – 0.6 V *vs.* Li$^+$/Li that is attributed to the delithiation of Li-Ge alloys. Furthermore, a shoulder was observed at voltage of 1.10 V *vs.* Li$^+$/Li corresponding to the oxidation of Ge to higher oxidation state. Further examination of discharge and charge plateaus on GCD profiles for the composites of Ge50 and Ge75 reveals similarities with their respective reduction and oxidation peaks in the CV profiles.

The voltage profiles of GeO_2/Ge/r-GO composite displayed impressive results. Firstly, Ge25 displayed 345 mAh/g and 272 mAh/g for initial specific capacity for discharge and charge at 100 mA/g, respectively as seen in Fig. 7.a. Cycling stability profiles of the Ge25 composite (see Fig. 7.b) revealed an initial coulombic efficiency (CE) of 78.8% that progressed towards 95 – 100% after 10 cycles and an average capacity retention of 91% after 100 cycles. The high initial CE and the excellent capacity retention of Ge25 indicated that the incorporation of 25% Ge in the r-GO framework resulted in stable electrochemical performance of the composite material compared to r-GO and other carbonaceous materials [65–68]. The voltage profile, as seen in Fig. 7.a, depicted an increase in the specific charge capacity of Ge25 anode, whilst the specific discharge capacity decreases as more cycling occurs. The average specific capacity was retained at around 300 mAh/g (1600 mAh/g calculated based on Ge content) over 100 cycles. This value is close to those reported in literature for diverse-dimensional carbon materials [69] and higher than porous reduced graphene oxide [70].

The voltage profiles for the Ge50 composites show improved specific capacity compared to that of Ge25. The profile displays initial discharge and charge capacities of 480 mAh/g and 376 mAh/g, respectively (Fig. 7.c). The cycling stability further supports the data provided by other GCD profiles, but also highlights a CE of above 90%, with a capacity retention of 71.4% after 50 cycles from 420 mAh/g to 300 mAh/g (Fig. 7.d). The Ge50 composites displayed improved specific capacity at the cost of capacity retention. The increase in the specific capacity can be attributed to the increase in Ge wt%, while the decrease in cycling stability can be traced back to the lower r-GO content. Unlike the Ge25 composite, a decrease in the r-GO content limits the nanosheets' ability to act as a conductive and supporting framework [71]. This trend is further continued towards Ge75 composites with a much higher Ge and lower r-GO contents. The voltage profiles of the Ge75 composite shows even more increase in specific capacity at the cost of poor cycling stability. A specific discharge and charge capacity was obtained at 630 mAh/g and 575 mAh/g, respectively as seen in Fig. 7.e and f. The cycling stability profile for the Ge75 shows decreased performance from a

specific capacity of 443 mAh/g to 188 mAh/g after 50 cycles resulting in 57.5% capacity retention (Fig. 7.f). In comparison to similar composites, the as synthesized GeO_2/Ge/r-GO composites do not perform with poorer electrochemical performance. Koo and Paek [27] reported that Ge/GeO_2/MRGO material reached average specific capacity of 1080 mAh/g (calculated based on Ge content) at 100 mA/g after 100 cycles. Wang et. al. reported that Ge@C/r-GO hybrid material exhibited a specific charge capacity of 1074.4 mAh/g (calculated based on Ge content) at 2 C (1 C = 1600 mA/g) after 600 cycles [72]. The high electrochemical performance of Ge/GeO_2/MRGO and Ge@C/r-GO hybrid materials have been explained by the accommodation of the volume change and improvement of electronic conductivity of r-GO framework [27],[72].

Closer scrutiny on the effects of Ge mass loading were heavily depicted in the comparative capacity retention change with the GCD cycles presented in Fig. 8.a. The plot compared the cycling stability of the three composites over a span of 50 cycles. The Ge25 composite started from an initial capacity retention below 90% but sharply increased after 7 cycles before finally stabilizing at 99%. Unlike the composites of Ge25 with a stable retention and the later discussed Ge75, the Ge50 composites did not follow the same declined progression. Instead, the capacity retention of the Ge50 composite had a gradual decline starting from 94% capacity retention down to 78.2% after 50 cycles. The Ge75 composite started at 85% which increased up to 100% on the 7th cycle followed by a more severe decline in the cycling retention as compared to both Ge50 and Ge25 composites. Overall, an increase in the Ge mass loading causes significant impairments on the cycling retention of the GeO_2/Ge/r-GO. The severe capacity fade demonstrated by the Ge75 highlights its ineffective capability in terms of a practical battery material, despite the improved specific capacity performance. Whereas the Ge25 had marginal improvements in specific capacity with exceedingly good capacity retention which limits its use as high energy capacity battery material. As such, the compromising performance demonstrated by the Ge50 composites indicate better practical usage with both improved specific capacities and a more lenient capacity fade.

The rate capability of the Ge50 composite was studied to better understand the electrochemical performance of the material at different current densities. As seen in Fig. 8.b, the Ge50 composite was subjected to electrochemical charge and discharge at current densities of 50, 100 and 200 mA/g from a voltage potential of 50–200 mV *vs.* Li$^+$/Li. The current density profile shows that an increase in current density from 50 to 200 mA/g causes a decrease in the specific discharge capacity from 503, 438 and 314 mAh/g, respectively. This is also exhibited for the specific charge capacity with a decrease from 473, 390 and 290 mAh/g as the current density increases. Comparatively, there is an approximate percentage decrease for specific discharge and charge capacities from 50 mA/g to 100 mA/g by 15% followed by a 27% decrease from 100 mA/g to 200 mA/g. The information provided indicates the composite's ability to perform at higher current densities. Moreover, Fig. 8.c, highlights the rate capability of the Ge50. The rate capability profile was similarly conducted over a span of 40 cycles initially starting from a current density of 50 mA/g followed by 100 and 200 mA/g before returning to 50 mA/g. The rate capability profile supports the information of a dramatic decrease in performance in the transition from 100 to 200 mA/g from 370 to 295 mAh/g, respectively. However, returning to the final current density 50 mA/g, the Ge50 composite behaved like the initial stages at 50 mA/g with a specific charge capacity of 408 mAh/ g. This is an indication of good rate capability performance on the Ge50 composite.

Due to the excellent capacity retention of the Ge25 composite, higher current density longitudinal cycling studies performed on the composite material at 400 mA/g over 500 cycles. Fig. 8.d highlights that even at a high current density of 400 mA/g, the Ge25 composite performs well with a CE of 99% and a capacity fade of 67% over 500 cycles from 110 to 74 mAh/g. The cyclability of Ge based anodes have always shown
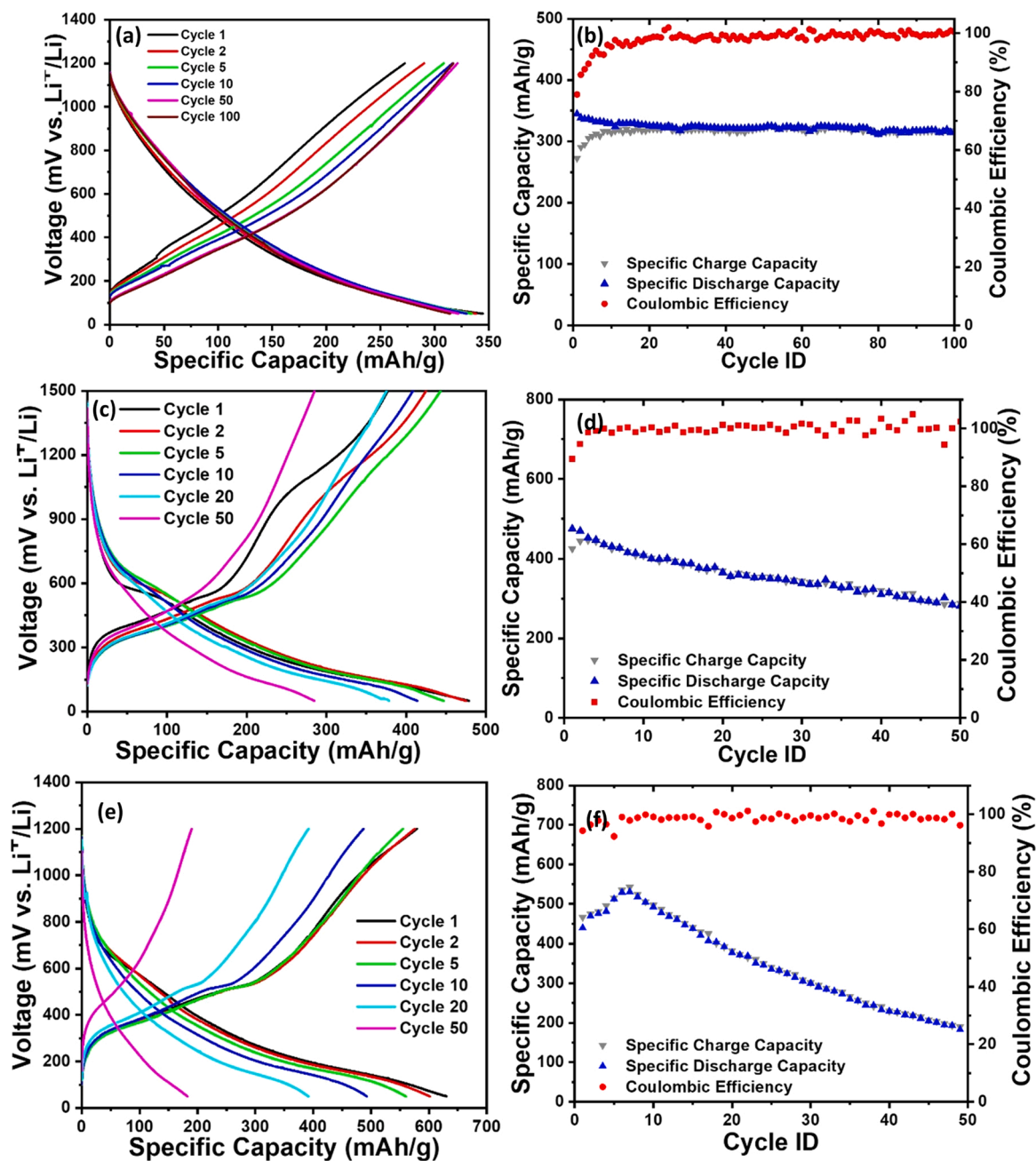
Fig. 7. GCD and cycling profiles conducted at 100 mA/g for (a) & (b) GeO$_2$/Ge25/r-GO, (c) & (d) GeO$_2$/Ge50/r-GO and (e) & (f) GeO$_2$/Ge75/r-GO.

difficulty over long terms [71,73,74]. As seen, the as-synthesized composite performs admirably as compared to previous studies such as that made by Ren et. Al, which proposed a Ge-graphene composite by thermal evaporation method with a specific capacity of 675 mAh/g (calculated based on Ge content) after 400 cycles at a current density 400 mA/g [54]. Work done by Xu et. al. further supports the ability of the r-GO matrix as a conductive and supporting framework that alleviates the degenerative Ge pulverization [71].

3.4. Postmortem analysis

3.4.1. XRD

To be able to fully understand the results obtained in the electrochemical characterization and performance, XRD studies were conducted for phase characterization to identify the formation of new products and phases at the three stages of ESF, PD (lithiated) and PC

(delithiated) for all three Ge mass loading composites. It can be seen from the three subsections, the plotlines for the composites deteriorated at increasing Ge mass loading. This pattern is not consistent with the comparative profiles at the PD and PC stage, thus cannot be related back to the effect of Ge mass loading. Fig. 9 depicts comparative XRD spectral profiles at the three different stages for each composite sample. Fig. 9.a, b and c showed the differences in peak intensities and peak locations between each stage. Fig. 9.a depicts a comparative profile of theGe25, Ge50 and Ge75 composites at the ESF stage. At the ESF XRD comparative profiles, with increasing mass loading of Ge, it was registered that most of the Ge component detected was found to be in cubic structure of space group *Fd3m* (JCPDS: 98–018–4252) for Ge25 and Ge50; however, at Ge75 the dominant structure of the Ge component shifted to hexagonal crystal structure of space group R3 (JCPDS: 98–024–5957). GeO$_2$ was also detected throughout all the composites in ESF stage with hexagonal crystal structure of space group *P3121* with no change
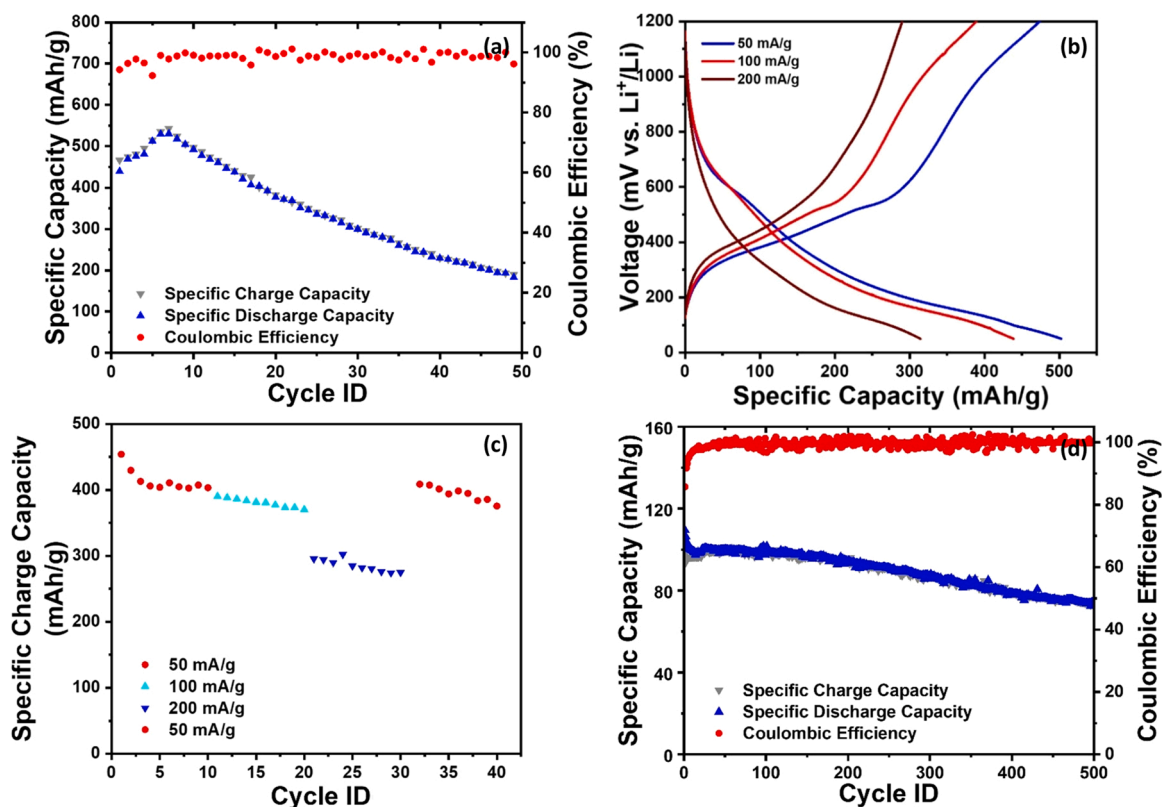
Fig. 8. (a) Cycling Stability of the three composites up to 50 cycles at 100 mA/g, (b) Current density studies, (c) rate capability studies for GeO$_2$/Ge/r-GO up to 40 cycles from 50 to 200 mA/g and (d) The Performance GeO$_2$/Ge50/r-GO at high rate / charge density of 400 mA/g for specific capacity and coulombic efficiency The Performance GeO$_2$/Ge50/r-GO at high rate / charge density of 400 mA/g for specific capacity and coulombic efficiency.

(JCPDS: 98–001–6577). For the comparative profile of GeO$_2$/Ge/r-GO on the PD stage (see Fig. 9.b), the Ge component registered to different crystal structures according to the database matching. At the Ge25 composite subsection, highest corresponding match belonged to hexagonal Ge (JCPDS: 98–024–5957) with less similarity to tetragonal Ge which also appeared in the potential Ge matches. This phenomenon is also seen in the Ge50 where the Ge component paired with hexagonal crystal structured Ge as opposed to the weaker Ge in cubic and tetragonal crystal structures. Interestingly, at the Ge75 subsection the crystal structure of Ge shifts back to cubic structure as opposed to the Ge crystal structure found in Ge25 and Ge50. During delithiation in the PC stage, the comparative XRD profiles showed the transition from hexagonal crystal structure for Ge25 and cubic Ge for Ge50 and Ge75 as seen Fig. 9.c. As mentioned earlier, the postmortem XRD profiles of the composites experience deterioration. This is especially clear for composite samples in the PD and PC stages and could be the result of amorphization of the GeO$_2$/Ge/r-GO composite, the result of interference from additives and the washing solvent or the result of diffusion induced stresses (DISs) leading to uncontrolled side reactions and mechanical fatigue [56,75]. The poor peak resolution seen in the PD and PC XRD profiles pose a challenge to make comparisons to see the effect of Ge mass loading on the structure of GeO$_2$/Ge/r-GO anode materials.

Although the deterioration of the postmortem XRD profiles made it difficult to study the effect of Ge mass loading, phase characterization was still applicable. When comparing the XRD profile subsections of the Ge25 composite at the three stages, it can be noticed that there are re-occurring peaks at certain regions such as at 2θ = 28.3° belonging to GeO$_2$ (see Fig. S.5.a). However, there is also a greater commonality between the PC and PD XRD plotlines with regards to the peaks found at 28.3°, 32.4°, 40.5°, 43.4° and 47.2° (see Fig. S.5.a). Further examination of the individual XRD plots (see Figs. S.5.d, S.5.g, S.5.j) revealed that the peak formation at 28.3° belongs to GeO$_2$ whilst the peaks at 32.4° and

47.2° correspond to Ge. The peak found at 40.5° could be the result of the diffraction pattern of the carbon additives used during slurry preparation in consideration of the consistent presence throughout all conducted postmortem XRD profiles whilst the sharpness of the peak suggests carbon is present in a crystalline phase [76–78]. The peak referenced at 43.4° was assigned for the alloy formation of Ge$_4$Li$_{15}$, which produced noticeable intensity in the PD XRD profiles and minor intensity in the PC XRD profiles for the Ge25 subsection. At the PD stage, the alloy formation of Ge$_4$Li$_{15}$ coincides with the alloying-mechanism proposed in the previous CV profile studies [79]. However, the reoccurring weak presence of the same peak at 43.4° on the PC XRD of Ge25 section suggests incomplete de-alloying of Ge$_4$Li$_{15}$. A closer look at the individual PD XRD profile of the Ge25 composite (see Fig. S.5.j) further shows unique peaks of Ge$_4$Li$_{15}$ detected at 20.2°, 74.2° and 90.03° which are not detected in the individual PC XRD profile (see Fig. S.5.g). The XRD profiles for the Ge50 composite also exhibited the same behavior as that in the previous XRD profiles with Ge25 composite where there was a higher degree in crystallinity in the ESF stage as compared to that of the PD and PC stages, albeit with less disparity. As seen in Fig. 9.a, b, and 9.c, the comparative XRD profiles showed poorer degree of crystallinity from the PD and PC plots for the Ge50 composite. This could be the result of the amorphization of the composite [80]. However, there are still distinguishable peak patterns for GeO$_2$ which can be found at 20.6°, 26.3°, 28.3° and 35.9°, whilst the peaks detected for Ge are found at 27.42°, 32.5° and 45.4°. The increased detected presence of Ge can be attributed to the increased Ge mass loading of the composite. Moreover, there is also the increased detected presence of GeO$_2$, which supports the claims mentioned during the CV analysis where the formation of GeO$_2$ surface films is more prevalent on the Ge microcubes. The individual PD XRD profile of Ge50 (see Fig. S.5.k) showed the dominating peak formations for Ge$_4$Li$_{15}$ at 26.0° and 43.3° followed by several weaker intensities of Ge and GeO$_2$. The Ge$_4$Li$_{15}$ peak
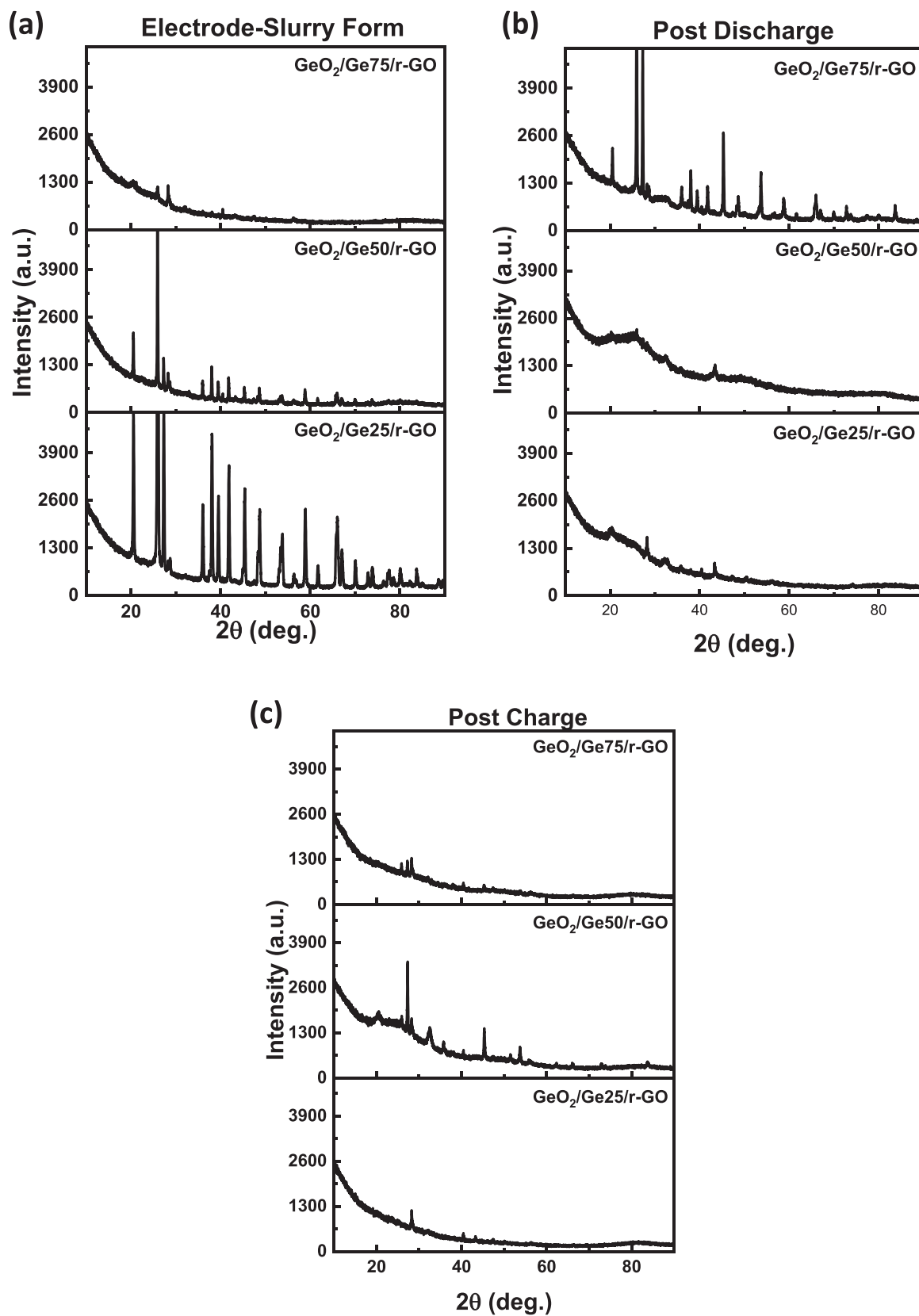
Fig. 9. Comparative Postmortem XRD profiles from $2\theta = 10° - 90°$ of the three composites at each stage **(a)** Electrode-Slurry Form (ESF), **(b)** Post Discharge (PD) and **(c)** Post Charge (PC).

formations were found to be limited to the PD XRD profile for Ge50 plot; however, it was also noticed that the peak region at approximately 26.0° is shared between both Ge_4Li_{15} as well as GeO_2. As such, the peak was present in both the ESF and PC XRD profiles for the Ge50 composite. Interestingly, the individual XRD profiles of Ge50 at PC stage indicated the presence of LiF at 38.1° as well as the repeated detected presence of Li_2O peaks throughout the PD and PC stage samples for all three composites which have characteristic peaks at 53.9° that both correspond to SEI formation [79,81]. SEI formation was A comparison of the Ge75 composite profiles functions as a better example that demonstrated the complete alloying and de-alloying of Ge_4Li_{15} in the PD and PC stages, respectively as seen in Fig. 9.b and c. Interestingly, the Ge75 composite exhibited better crystallinity and peak resolution in the PD stage as opposed to the ESF and PC stages. Although there is poor resolution in the other stages, peaks were detected for critical components of the composite material. Like the other composites, there are peaks detected for GeO_2 and Ge for all three stages on the XRD subsections of the Ge75 composite because of high Ge mass loading. There is also the repeated presence of LiF at 38.1°. More importantly, there is the clear distinguishable formation of Ge_4Li_{15} limited only to the PD stage. This is clear indication for alloying and de-alloying of Ge during discharge and charge.

3.4.2. SEM

To determine whether alloying and de-alloying mechanism provide visible morphological and structural changes on the surface, postmortem SEM was conducted on the same set of conditioned samples across three Ge mass loadings. Like the SEM micrographs of the material characterization of the composite, it can be seen in the postmortem micrographs at increasing mass loading of Ge, there is an increasing visual presence of the Ge microcubes on the surface structure. More importantly, there is an increased texture disturbance present on the overlaying r-GO framework. These additional textures, as seen in the postmortem micrographs, are the result of slurry additives, Lutfi cell electrolyte and propylene carbonate washing solvent on the surface of the anode composite – thus creating heavily texture dense SEM micrographs. The SEM postmortem micrographs of the Ge25 composites indicated very weak indication for the presence of the Ge microcubes within the r-GO framework. Due to the overwhelming presence of the r-GO framework and further additives, there is the possibility of the Ge microcubes being further wrapped within the structure, hence a lack of visibility. However, Fig. S.6.b of the PD Ge25 micrograph at high magnification showed very noticeable clusters formation occurring that are not present in the ESF and PC micrographs which have more random textures. These noticeable clusters could be attributed to the microcubes undergoing volumetric expansion during discharge stages. In which, the isolated clusters formation of Ge microcubes hidden within the structure forcibly expand against the r-GO framework and additive layers. At higher Ge mass loading, the postmortem micrographs depict more distinguishable features for the Ge50 composite. As seen in Fig. 10, there is a greater presence of Ge microcubes within the composite framework. Fig. 10.**a, b** and c of the three SEM postmortem micrographs for the Ge50 composite showed there is no noticeable presence of the Ge microcubes within the PC micrograph, however between the ESF and the PD micrographs there was a noticeable change. The microcubes present in the ESF and PD micrographs have shown considerable dimensional size difference with a growth from approximately 1.3 to 2 μm from ESF to the PD stage. Moreover, the microcubes present in the SEM PD micrograph also exhibited cracking formation. This coincides with the volumetric expansion phenomenon and pulverization effect of Ge after electrochemical discharge [4–8]. The growth of these microcubes could be attributed to the alloy formation of Ge_4Li_{15} detected

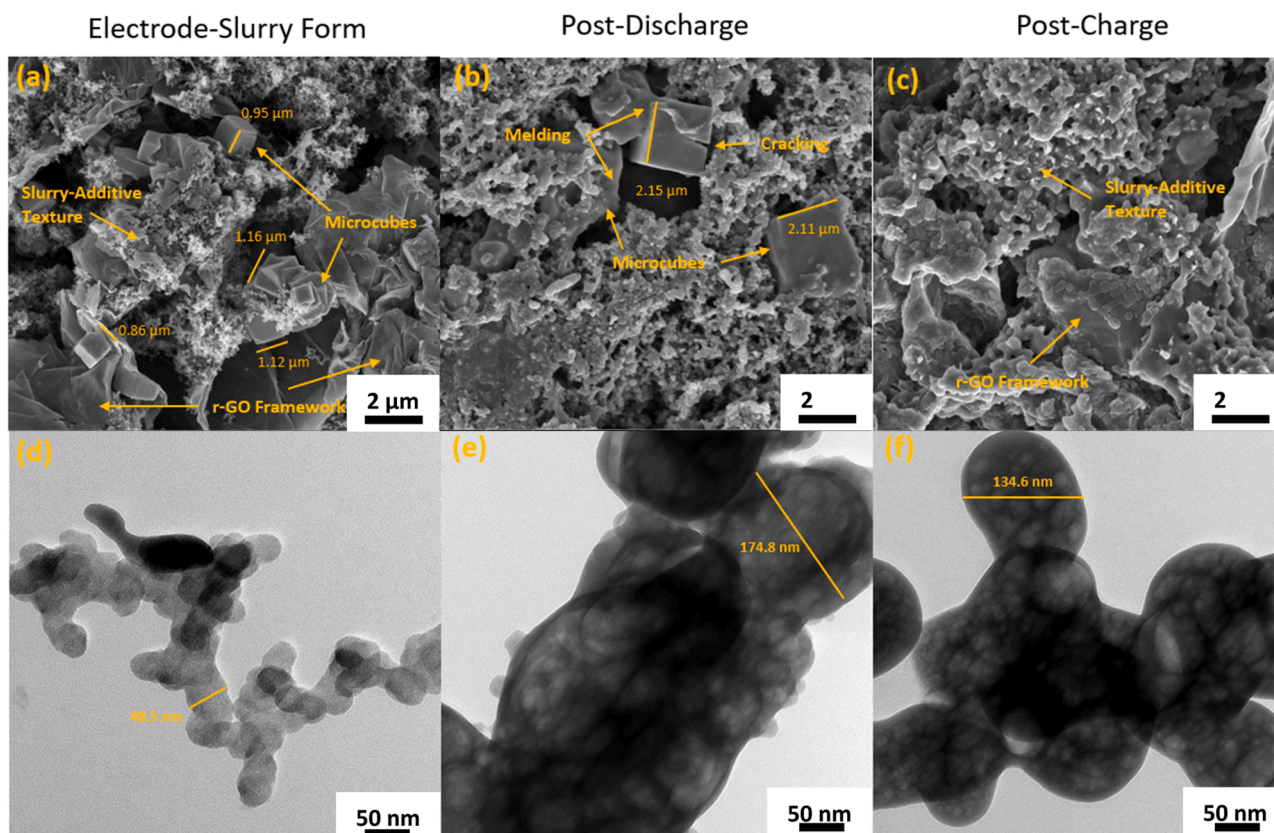**Fig. 10.** SEM Postmortem micrographs of the GeO_2/Ge50/r-GO composite taken at uniform scale length of 5 μm for the three stages; (a) ESF, (b) PD and (c) PC used as clear indication of microcube presence and post GCD morphology. HR-TEM postmortem micrographs of the GeO_2/Ge50/r-GO composite at uniform scale length of 50 nm for the three stages; (d) ESF, (e) PD and (f) PC.

during XRD phase confirmation of the composite at the PD stage, in which Ge undergoes alloying with Li. Further examination of the SEM micrographs at lower magnification reveals similar characteristics. The SEM ESF micrographs of the Ge50 composite revealed clustered microcube formations of Ge, but more importantly the size distribution of the microcubes was found to be relatively uniform at 1.1–1.2 μm as compared to the microcubes in the SEM PD micrographs of 2 μm in size. Aside from the increased size of the microcubes, there is also an uneven texture present on the surface of the microcubes as seen in the SEM PD micrograph. As can be seen on both the SEM postmortem micrographs of Ge25 and Ge50 at the PC stage, there is a general lack of presence of the microcubes. This could be related to the de-alloying of Ge_4Li_{15} into a different structure and size within the r-GO framework which makes it difficult to differentiate. Moreover, in the SEM PD micrograph of Ge50 at high resolution, there are slightly discernable cubic features melded onto the composite framework with similar size as compared to microcubes in the ESF stage at 1.13 μm (see Fig. S.7.b.). The SEM postmortem micrographs for Ge75 composite provided a clear representation for the morphological changes seen between the three stages. The SEM ESF micrograph showed Ge microcube clusters found with similar dimensions of 1.12 μm. Following into the PD stage, the SEM micrograph shows clusters of microcubes with dimensions of approximately 2 μm indicating growth due to Ge expansion. More interestingly, there is clearer indication that during the electrochemical charge-discharge process, the microcubes appear to be further melded into the framework making it difficult to discern as seen in the SEM PD micrographs as previously seen in SEM micrographs of the Ge50 composite. This is in support of the previous notion described in the SEM micrographs of Ge50 and could explain the lack of microcube features in the SEM PC micrographs. The semi-melded microcubes also appear to have grainier textures on the cube surface, which suggests SEI formation or potentially the formation of the Ge_4Li_{15} alloy. Furthermore, the cracking present on the microcube surface during PD correspond to the pulverization and structural degradation of Ge with respect to electrochemical charge-discharge. The PC SEM micrographs taken for the Ge75 composite show a completely flat surface.

3.4.3. TEM

Post-mortem TEM was conducted to confirm the results obtained from post-mortem XRD and SEM regarding the phase-crystal structures and morphology dimensional changes, respectively. Post-mortem TEM micrographs all depicted encapsulated Ge within the r-GO framework of the GeO_2/Ge/r-GO composites at the ESF, PD and PC stages. The TEM ESF micrographs of the Ge25 composite shows low Ge compactness within the r-GO framework at low Ge mass loadings of 25% (see Fig. S.9). When the postmortem micrographs of Ge25 at the three different stages are compared, there is a very noticeable difference in the size of the encapsuled structure. The micrographs at 100 nm scale, highlights encapsuled approximate average sizes of 48.8 nm, 76 nm, and 63.4 nm for ESF, PD and PC, respectively. This size growth is related to the response of the Ge microcubes with respect to electrochemical charge and discharge. At the ESF stage the encapsuled structure had average length of 48.8 nm, followed by the lithiation of Ge (PD) within the encapsulant leading to size growth up to 76 nm. The reduction in size from PD to PC of 63.4 nm refers to the delithiation of Ge (PC) within the encapsulant structure. This phenomenon is clearly seen within the TEM micrographs of both 100 nm and 50 nm scales. At higher Ge mass loadings of 50%, the TEM micrographs for the Ge50 component showed more extreme size changes between the three stages. From ESF, to PC and finally PD, the TEM micrographs revealed approximate encapsulant framework sizes of 40 nm, 140 nm, and 170 nm, respectively. The initial encapsulant size at ESF can be attributed to growth effect of Ge while the severe growth change between the three stages could be related to the increased Ge mass loading of the composite. The increased Ge mass loading results in a higher density packing of Ge within the encapsulant r-GO framework, leading to greater size changed when compared to the

Ge25 composite of lower density packing. The increased Ge density packing can be clearly seen in Fig. 10.**d, e,** and f, where there are higher concentrations of Ge spheres within the encapsulant. On the TEM ESF micrograph of Ge50, there is a noticeable lack of Ge component within the framework as opposed to the enlarged Ge spheres within encapsulant at the PD and PC stages. The TEM micrographs for Ge75 provided a perspective of more isolated clusters of Ge encapsuled in the r-GO framework. Fig. S.11 represents the TEM micrographs at a scale of 50 nm, which showed similar encapsulant structures but with no discernable interior smaller spheres of Ge as seen with the TEM micrographs of the Ge25 and Ge50 composites. Instead, there are darker whole body regions that overlap with the encapsulant structure. This could be the result of even higher density packing within the encapsulant, leading to darker regions on the TEM micrographs. Fringing patterns were conducted on the darker regions at higher resolutions of the TEM PD micrographs to confirm the identity through crystal spacing. Fringes revealed a ᴅ-space value of 3.3 Å which coincides with lattice space (310) for Ge_4Li_{15} [82] (see Fig. S.12). This resolved the suspicion of Ge-Li alloys detected during postmortem XRD and supports the assumptions from the postmortem SEM results. Further support from TEM fringing of the composite material at ESF (see Fig. S.13) highlighted the formation of Ge component with ᴅ-spacing of 3.2 Å, corresponding to lattice planes (111). These also confirmed the representation of the enlarged dark bodies as part of the Ge component. Like the previous TEM micrographs of the other composites, there is a noticeable size difference seen within the three stages. From the ESF to initial PD, there is a size increase followed by a size decrease to the initial PC stage. The size transitions correspond to lithiation and delithiation of the encapsuled Ge component. Although there are differences in the size changed between the three Ge mass loadings, the pattern of increase followed by decrease from ESF to PD and from PD to PC prevail. However, it should be noted that the delithiation transition of the PC stage does not return the structure size back to that found on the TEM ESF micrographs, which indicates that the delithiation from PD to PC did not go to full completion or a larger crystalline structure did form.

3.4.4. XPS

XPS was used due to its ability study the surface of the material as well as the chemical bonding compositions present. The technique was performed on a sample of Ge50 composite, at the three conditions, which was selected due to its balanced performance during the electrochemical studies and for providing ample results in the previous postmortem studies. Fig. S.14 depicts a broad scan XPS spectra of the Ge50 composite from 0 to 1200 eV which showed multiple strong signals pertaining to Ge 3d, Ge 3p, Ge 3 s, C 1 s, Ge LMM, O 1 s, Cu LMM, F 1 s, F KLL and O KLL [45,83–85]. The extreme signals belonging to the O 1 s and F 1 s are explained to be the result of significant GeO_2 and oxide formation, which includes the SEI layer, on the surface of the composite material and are further discussed later. This increased intensity brought about by the surface oxides and SEI layer resulted in the detection weakening of other chemical compositions, resulting in limited XPS signal resolution.

Detailed spectra belonging to the Ge 3d region from 20 to 40 eV showed multiple strong signals as seen in Fig. S.14. Resolved peaks were determined to be Ge-Ge and Ge-O bonds corresponding to postmortem XRD profiles on the GeO_2/Ge/r-GO composite. The Ge-Ge binding energy was resolved and found to be at 30.3, 30.4 and 29.4 eV for ESF, PD and PC, respectively and matched with literature values [83–89]. More importantly, the Ge-Ge signal intensity detected in the ESF stage was significantly weaker compared to the PD and PC stages as seen in Fig. 11. a, b and **c** This suggested that the majority of Ge component on the surface of the microcubes during ESF belonged to GeO_2. A signal belonging to Ge-O (GeO_2) was resolved at the three stages with binding energy of 33.6, 31.7 and 31.1 eV for ESF, PD and PC, respectively [83–89]. When comparing the distribution of the resolved curves, in the PD stage the Ge-Ge signal contributes a greater proportion as compared
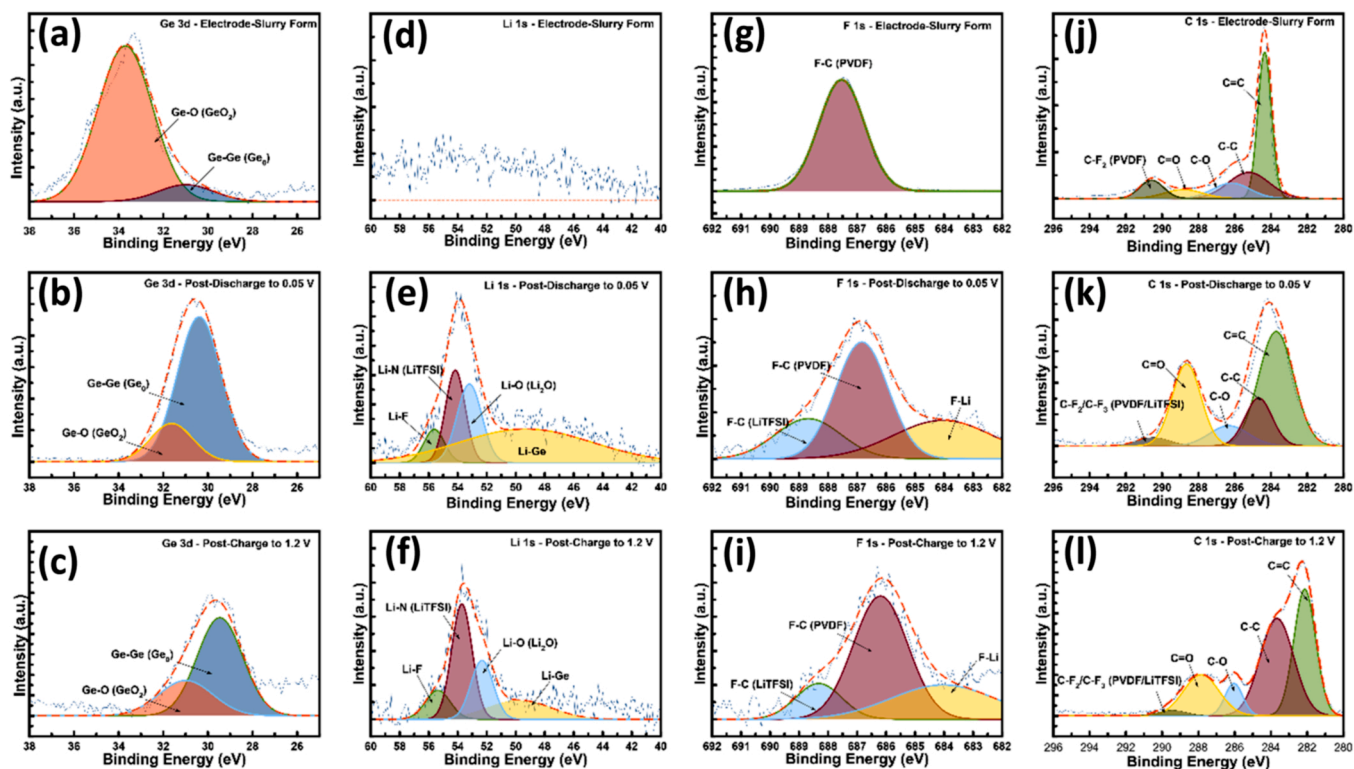
Fig. 11. Postmortem high resolution XPS of GeO$_2$/Ge50/r-GO indicating surface chemical compositions and changes at specified spectra: Ge 1 s (a) ESF, (b) PD and (c) PC. Li 1 s at (d) ESF, (e) PD and (f) PC. F 1 s (g) ESF, (h) PD and (i) PC. C 1 s (j) ESF, (k) PD and (l) PC.

to the Ge-O signal. This can be attributed to the conversion of GeO$_2$ to Ge and Li$_2$O during the discharge phase [27,55,57,90]. The Ge 3d XPS spectra at the PC stage depicted an increased contribution of the resolved Ge-O signal as part of the broad signal which corresponds to the oxidation of Ge to GeO$_2$ in the charge phase. A dramatic signal shifting was observed for Ge-Ge to lower binding energy between the ESF and PC/PD stages. Literature suggested this could be the result of the formation of the Li$_x$Ge alloy during the PD stage, with residual Li$_x$Ge alloys not de-alloying after charging to 1.2 V [57].

A detailed spectra of the Li 1 s region was also obtained and the broad peak located at approximately 53.5 eV was deconvoluted for the composite at the three stages as seen in Fig. 11.d, e and f. The Li 1 s spectra at ESF displayed no significant signals, however at the PD and PC stage four peaks were resolved. Signals belonging to the formed SEI layer were detected for Li-F at 55.6 and 55.4 eV, and Li-O (Li$_2$O) signals at 53.2 and 52.3 eV paired for the PD and PC stages, respectively, which coincides with previous postmortem XRD findings [83,91,92]. Like the GeO$_2$ signal contribution, Li-O signal contribution to the broad peak was much greater in the PD stage as opposed to the PC stage. This is related to the formation of Li$_2$O from the reduction of GeO$_2$ [27,55,57,90]. A signal was also resolved for Li-N at 54.1 and 53.7 eV for PD and PC stages, respectively. This signal was reported to be the LiTFSI electrolyte in literature [93]. More interestingly, the Li 1 s spectra depicted a broad tail located approximately at 50 eV. This broad tail was deconvoluted with the other chemical bonds to produce a signal found at 49.3 for the PD stage and 49.7 for the PC stage. As a result of a lack of presence during ESF and greater signal presence in the PD stage than in the PC stage, it is suspected that this resolved signal potentially belongs to Li-Ge alloys formed. This is in conjunction with results from Ge 3d region as well as from postmortem TEM fringing and XRD.

Strong signals belonging to the PVDF and LiTFSI components were deconvoluted in the F 1 s detailed spectra of the composite as seen in Fig. 11.g, h and i. The deconvoluted signals for F-C of the LiTFSI component were found in the PD and PC stage at 688.7 and 688.3 eV,

respectively [91,94]. The PVDF F-C signals were resolved in all three stages ESF with 687.5 eV, PD with 686.8 eV and 688.3 eV for the PC stage [95,96]. F-Li signals were also determined 684.3 eV with no significant difference in the PD and PC stage [91,97,98]. All three signals match with literature values pertaining to the F 1 s. The XPS spectra of C 1 s was deconvoluted, and the peak distribution confirmed the formation of the r-GO framework as previously seen through Raman spectroscopy. The ESF C 1 s XPS spectra revealed similar deconvoluted signals corresponding to literature spectra of the r-GO component with bonds of 284.3, 285.2, 286.2 and 288.8 eV for C=C, C-C, C-O and C=O, respectively as seen in Fig. 11.j, 11.k and 11.l [99,100]. C-F$_2$ bond pertaining to the PVDF slurry additive was also detected at approximately 290.5 eV for all three stages [95,96]. C-F$_3$ signals from LiTFSI were determined and found slightly overlapping with the C-F$_2$ signal PVDF ranging from 291 to 292 eV, limited only in the PD and PC stages [91,101,102]. The C 1 s spectra of the PD and PC stage exhibited severe lower binding energy shifting and peak broadening as compared to the spectra of ESF. Fig. S.15.a, b and c depicts the O 1 s XPS spectra at the three stages. The broad signal centered at 532 eV was deconvoluted into four signals at 531.5, 531.7, 532.8 and 534.9 eV for the C=O, O-Ge, C-O and O-H bonds, respectively. The O-Ge signal corresponds to the formation of GeO$_2$ which increases in signal contribution at the PC stage with the oxidation of Ge [45,103]. The broad signal in the 530–534 eV range exhibited lower binding energy shifts after the PD stage to 530.46 eV and PC stage to 529.16 eV. This phenomenon could be attributed to the development of O-S (LiTFSI) and the more specifically the O-Li signals at lower binding energies found at 530.4 and 529 eV for PD stage, and 529.1 and 528.5 eV for the PC stage [102,104,105].

4. Conclusion

GeO$_2$/Ge/r-GO composites were synthesized by using a controlled microwave irradiation of ball-milled Ge and sonicated dispersion of GO at three Ge weight percentages to study the changes in electrochemical

performance. Material Characterization of SEM and TEM revealed the formation of microcube structures encapsulated within a layer of r-GO, whilst XRD and EDX confirmed the phase-pure composition of the as-synthesized composite, specifically the differences between the GeO_2 and Ge components across the three Ge wt% samples, whilst Raman spectroscopy was used to confirm the transformation of GO to r-GO by means of the I_D/I_G ratio of 1.22. Electrochemical characterization by cyclic voltammetry of the composite anode hints at the changes of the lithiation and delithiation mechanism with respect to increase Ge mass loading, shifting from Li^+ intercalation/de-intercalation with the r-GO framework to Ge alloy/de-alloying. GCD of the three composites showed that at 25% Ge mass loading, the anode performed with excellent cycling retention of 91% after 100 cycles and an average specific capacity of 300 mAh/g (1600 mAh/g with respect to mass of Ge and rate of 100 mA/g), whilst the composite at 75% Ge mass loading performed with improved specific discharge capacity of 630 mAh/g (rate of 100 mA/g) albeit with poor cycling retention of 57.5% in 50 cycles. Our study shows that a balance was reached at Ge mass loading of 50% with both stable cycling retention of 71.4% after 50 cycles and good specific discharge capacity value of 480 mAh/g at a current density of 100 mA/g. Further GCD studies reveal stable cycling retention even at higher current density of 400 mA/g pertaining to 25% Ge mass loading with a coulombic efficiency of 99% and a capacity fade of 67% over 500 cycles. Postmortem analysis at the ESF, PD and PC stages of the Ge50 composite by TEM and SEM show the morphological changes of the microcube structures exhibiting a semi-melded appearance into the r-GO framework, while XRD and XPS confirm the presence of Li_xGe_y alloy formation.

CRediT authorship contribution statement

Nasr Bensalah: Conceptualization, Methodology, Validation, Data curation, Resources, Project administration, Writing – review & editing, Supervision. **Christian Randell Arro:** Investigation, Formal analysis, Data curation, Writing – original draft. **Assem Taha Ibrahim Mohamed:** Investigation, Methodology, Validation, Data curation.

Declaration of Competing Interest

The authors declare that they have no known competing financial interests or personal relationships that could have appeared to influence the work reported in this paper.

Acknowledgements

Appendix A. Supporting information

Supplementary data associated with this article can be found in the online version at doi:10.1016/j.mtcomm.2022.103151.

References

[1] Global E.V.Outlook 2020, Glob. EV Outlook 2020, 2020). https://doi.org/10.1787/d394399e-en.

[2] C. Xu, Q. Dai, L. Gaines, M. Hu, A. Tukker, B. Steubing, Future material demand for automotive lithium-based batteries, Commun. Mater. 1 (2020), https://doi.org/10.1038/s43246-020-00095-x.

[3] H.J. Kim, T.N.V. Krishna, K. Zeb, V. Rajangam, C.V.V. Muralee Gopi, S. Sambasivam, K.V.G. Raghavendra, I.M. Obaidat, A comprehensive review of li-ion battery materials and their recycling techniques, 2020. https://doi.org/10.3390/electronics9071161.

[4] W. Li, X. Sun, Y. Yu, Si-, Ge-, Sn-based anode materials for lithium-ion batteries: from structure design to electrochemical performance, Small Methods 1 (2017) 22–30, https://doi.org/10.1002/smtd.201600037.

[5] S. Liu, J. Feng, X. Bian, Y. Qian, J. Liu, H. Xu, Nanoporous germanium as high-capacity lithium-ion battery anode, Nano Energy 13 (2015) 651–657, https://doi.org/10.1016/j.nanoen.2015.03.039.

[6] Z. Hu, S. Zhang, C. Zhang, G. Cui, High performance germanium-based anode materials, Coord. Chem. Rev (2016) 34–85, https://doi.org/10.1016/j.ccr.2016.08.002.

[7] J.G. Ren, Q.H. Wu, H. Tang, G. Hong, W. Zhang, S.T. Lee, Germanium-graphene composite anode for high-energy lithium batteries with long cycle life, J. Mater. Chem. A. 1 (2013) 1821–1826, https://doi.org/10.1039/c2ta01286c.

[8] X. Li, Z. Yang, Y. Fu, L. Qiao, D. Li, H. Yue, D. He, Germanium anode with excellent lithium storage performance in a germanium/lithium-cobalt oxide lithium-ion battery, ACS Nano 9 (2015) 1858–1867, https://doi.org/10.1021/nn506760p.

[9] H. Zhang, Y. Yang, D. Ren, L. Wang, X. He, Graphite as anode materials: fundamental mechanism, recent progress and advances, Energy Storage Mater. 36 (2021) 147–170, https://doi.org/10.1016/j.ensm.2020.12.027.

[10] H. Cheng, J.G. Shapter, Y. Li, G. Gao, Recent progress of advanced anode materials of lithium-ion batteries, J. Energy Chem. 57 (2021) 451–468, https://doi.org/10.1016/j.jechem.2020.08.056.

[11] J. Asenbauer, T. Eisenmann, M. Kuenzel, A. Kazzazi, Z. Chen, D. Bresser, The success story of graphite as a lithium-ion anode material – fundamentals{,} remaining challenges{,} and recent developments including silicon (oxide) composites, Sustain, Energy Fuels 4 (2020) 5387–5416, https://doi.org/10.1039/D0SE00175A.

[12] C. Lee, Y.-J. Han, Y.D. Seo, K. Nakabayashi, J. Miyawaki, R. Santamaría, R. Menéndez, S.-H. Yoon, J. Jang, C4F8 plasma treatment as an effective route for improving rate performance of natural/synthetic graphite anodes in lithium ion batteries, Carbon N. Y 103 (2016) 28–35, https://doi.org/10.1016/j.carbon.2016.02.060.

[13] J.-S. Yeo, T.-H. Park, M.-H. Seo, J. Miyawaki, I. Mochida, S.-H. Yoon, Enhancement of the rate capability of graphite via the introduction of boron-oxygen functional groups, Int. J. Electrochem. Sci. 8 (2013) 1308–1315.

[14] T.-H. Park, J.-S. Yeo, M.-H. Seo, J. Miyawaki, I. Mochida, S.-H. Yoon, Enhancing the rate performance of graphite anodes through addition of natural graphite/carbon nanofibers in lithium-ion batteries, Electrochim. Acta 93 (2013) 236–240, https://doi.org/10.1016/j.electacta.2012.12.124.

[15] S. Liang, Y.-J. Cheng, J. Zhu, Y. Xia, P. Müller-Buschbaum, A Chronicle review of nonsilicon (Sn, Sb, Ge)-based lithium/sodium-ion battery alloying anodes, Small Methods 4 (2020), 2000218, https://doi.org/10.1002/smtd.202000218.

[16] H. Tian, F. Xin, X. Wang, W. He, W. Han, High capacity group-IV elements (Si, Ge, Sn) based anodes for lithium-ion batteries, J. Mater. 1 (2015) 153–169, https://doi.org/10.1016/j.jmat.2015.06.002.

[17] D. Liu, Z. jiao Liu, X. Li, W. Xie, Q. Wang, Q. Liu, Y. Fu, D. He, Group IVA element (Si, Ge, Sn)-based alloying/dealloying anodes as negative electrodes for full-cell lithium-ion batteries, Small 13 (2017) 1–27, https://doi.org/10.1002/smll.201702000.

[18] K. Huo, L. Wang, C. Peng, X. Peng, Y. Li, Q. Li, Z. Jin, P.K. Chu, Crumpled N-doped carbon nanotubes encapsulated with peapod-like Ge nanoparticles for high-rate and long-life Li-ion battery anodes, J. Mater. Chem. A 4 (2016) 7585–7590, https://doi.org/10.1039/c6ta01972b.

[19] Y. Chen, L. Ma, X. Shen, Z. Ji, A. Yuan, K. Xu, S.A. Shah, In-situ synthesis of Ge/reduced graphene oxide composites as ultrahigh rate anode for lithium-ion battery, J. Alloy. Compd. 801 (2019) 90–98, https://doi.org/10.1016/j.jallcom.2019.06.074.

[20] L.P. Tan, Z. Lu, H.T. Tan, J. Zhu, X. Rui, Q. Yan, H.H. Hng, Germanium nanowires-based carbon composite as anodes for lithium-ion batteries, J. Power Sources 206 (2012) 253–258, https://doi.org/10.1016/j.jpowsour.2011.12.064.

[21] J. Doherty, D. McNulty, S. Biswas, K. Moore, M. Conroy, U. Bangert, C. O'Dwyer, J.D. Holmes, Germanium tin alloy nanowires as anode materials for high performance Li-ion batteries, Nanotechnology 31 (2020), 165402, https://doi.org/10.1088/1361-6528/ab6678.

[22] T. Kennedy, E. Mullane, H. Geaney, M. Osiak, C. O'Dwyer, K.M. Ryan, High-performance germanium nanowire-based lithium-ion battery anodes extending over 1000 cycles through in situ formation of a continuous porous network, Nano Lett. 14 (2014) 716–723, https://doi.org/10.1021/nl403979s.

[23] J. Zhou, Y. Zhou, X. Zhang, L. Cheng, M. Qian, W. Wei, H. Wang, Germanium-based high-performance dual-ion batteries, Nanoscale 12 (2020) 79–84, https://doi.org/10.1039/c9nr08783d.

[24] L. Deng, W. Li, H. Li, W. Cai, J. Wang, H. Zhang, H. Jia, X. Wang, S. Cheng, A hierarchical copper oxide–germanium hybrid film for high areal capacity lithium ion batteries, Front. Chem. 7 (2020) 869, https://doi.org/10.3389/fchem.2019.00869.

[25] T.D. Bogart, A.M. Chockla, B.A. Korgel, High capacity lithium ion battery anodes of silicon and germanium, Curr. Opin. Chem. Eng. 2 (2013) 286–293, https://doi.org/10.1016/j.coche.2013.07.001.

[26] X. Gao, W. Luo, C. Zhong, D. Wexler, S.L. Chou, H.K. Liu, Z. Shi, G. Chen, K. Ozawa, J.Z. Wang, Novel germanium/polypyrrole composite for high power lithium-ion batteries, Sci. Rep. 4 (2014) 1–8, https://doi.org/10.1038/srep06095.

[27] J.-H. Koo, S.-M. Paek, Microwave-assisted synthesis of Ge/GeO2-reduced graphene oxide nanocomposite with enhanced discharge capacity for lithium-ion batteries, Nanomaterials 11 (2021) 319, https://doi.org/10.3390/nano11020319.

[28] N. Zaaba, K. Foo, U. Hashim, W.-W. Liu, C. Voon, P. Besar, Synthesis of graphene oxide using modified hummers method: solvent influence, Procedia Eng. 184 (2017) 469–477, https://doi.org/10.1016/j.proeng.2017.04.118.

[29] D. Li, H. Wang, H.K. Liu, Z. Guo, A. New, Strategy for achieving a high performance anode for lithium ion batteries—encapsulating germanium nanoparticles in carbon nanoboxes, Adv. Energy Mater. 6 (2016), 1501666, https://doi.org/10.1002/aenm.201501666.

[30] D. Zhou, G. Chen, S. Fu, Y. Zuo, Y. Yu, Germanium photodetector with distributed absorption regions, Opt. Express 28 (2020) 19797–19807, https://doi.org/10.1364/OE.390079.

[31] Y. Wang, U. Ramesh, C.K.A. Nyamekye, B.J. Ryan, R.D. Nelson, A.M. Alebri, U. H. Hamdeh, A. Hadi, E.A. Smith, M.G. Panthani, Synthesis of germanium nanocrystals from solid-state disproportionation of a chloride-derived germania glass, Chem. Commun. 55 (2019) 6102–6105, https://doi.org/10.1039/c9cc01676g.

[32] X. Zhou, J. Xu, Y. Chen, D. Li, Geo2-coated MCMB composite as anode material for lithium ion battery in PC-based electrolyte, in: IOP Conf. Ser. Mater. Sci. Eng., Institute of Physics Publishing, 2018, https://doi.org/10.1088/1757-899X/452/2/022142.

[33] C. Jing, C. Zhang, X. Zang, W. Zhou, W. Bai, T. Lin, J. Chu, Fabrication and characteristics of porous germanium films, Sci. Technol. Adv. Mater. 10 (2009) 6, https://doi.org/10.1088/1468-6996/10/6/065001.

[34] S. Wang, X. Gu, L. Wang, C. Wu, Q. Liu, L. Zhao, Y. Xue, W. Li, Y. Rui, J. Xu, M. Ding, Design of rugby-like GeO 2 grown on carbon cloth as a flexible anode for high-performance lithium-ion batteries, J. Nanosci. Nanotechnol. (2018), https://doi.org/10.1166/jnn.2019.16455.

[35] B. Wang, Z. Wen, J. Jin, X. Hong, S. Zhang, K. Rui, A novel strategy to prepare Ge@C/rGO hybrids as high-rate anode materials for lithium ion batteries, J. Power Sources 342 (2017) 521–528, https://doi.org/10.1016/j.jpowsour.2016.12.091.

[36] P. Giri, S. Dhara, Core-shell nanocrystals with varying sizes and shell thicknesses: microstructure and photoluminescence studies, J. Nanomater 5 (2012), 905178, https://doi.org/10.1155/2012/905178.

[37] S. Muhammad Hafiz, R. Ritikos, T.J. Whitcher, N. Md. Razib, D.C.S. Bien, N. Chanlek, H. Nakajima, T. Saisopa, P. Songsiririthigul, N.M. Huang, S. A. Rahman, A practical carbon dioxide gas sensor using room-temperature hydrogen plasma reduced graphene oxide, Sens. Actuators B Chem. 193 (2014) 692–700, https://doi.org/10.1016/j.snb.2013.12.017.

[38] O.N. Koroleva, T.N. Ivanova, Raman spectroscopy of the structures of Li2O-SiO2 and Li2O-GeO2 melts, Russ. Metall. 2014 (2014) 140–146, https://doi.org/10.1134/S0036029514020098.

[39] B. Ma, R.D. Rodriguez, A. Ruban, S. Pavlov, E. Sheremet, The correlation between electrical conductivity and second-order Raman modes of laser-reduced graphene oxide, Phys. Chem. Chem. Phys. 21 (2019) 10125–10134, https://doi.org/10.1039/C9CP00093C.

[40] A. Kaniyoor, S. Ramaprabhu, A Raman spectroscopic investigation of graphite oxide derived graphene, AIP Adv. 2 (2012) 32183, https://doi.org/10.1063/1.4756995.

[41] R. Muzyka, S. Drewniak, T. Pustelny, M. Chrubasik, G. Gryglewicz, Characterization of graphite oxide and reduced graphene oxide obtained from different graphite precursors and oxidized by different methods using raman spectroscopy, Materials (2018), https://doi.org/10.3390/ma11071050.

[42] L. Xu, L. Cheng, Graphite oxide under high pressure: a raman spectroscopic study, J. Nanomater. 2013 (2013), 731875, https://doi.org/10.1155/2013/731875.

[43] A.R. Zanatta, Temperature-dependent Raman scattering of the Ge + GeOx system and its potential as an optical thermometer, Results Phys. 19 (2020), 103500, https://doi.org/10.1016/j.rinp.2020.103500.

[44] A. Lignie, P. Hermet, G. Fraysse, P. Armand, Raman study of α-quartz-type Ge1−xSixO2 (0 < x ≤ 0.067) single crystals for piezoelectric applications, RSC Adv. 5 (2015) 55795–55800, https://doi.org/10.1039/C5RA08051G.

[45] B. Wang, J. Jin, X. Hong, S. Gu, J. Guo, Z. Wen, Facile synthesis of the sandwich-structured germanium/reduced graphene oxide hybrid: an advanced anode material for high-performance lithium ion batteries, J. Mater. Chem. A 5 (2017) 13430–13438, https://doi.org/10.1039/C7TA03087H.

[46] T. Huang, Y. Yang, K. Pu, J. Zhang, M. Gao, H. Pan, Y. Liu, Linking particle size to improved electrochemical performance of SiO anodes for Li-ion batteries, RSC Adv. 7 (2017) 2273–2280, https://doi.org/10.1039/C6RA25714C.

[47] G. Xu, J. Han, B. Ding, P. Nie, J. Pan, H. Dou, H. Li, X. Zhang, Biomass-derived porous carbon materials with sulfur and nitrogen dual-doping for energy storage, Green. Chem. 17 (2015) 1668–1674, https://doi.org/10.1039/C4GC02185A.

[48] S. Maruyama, T. Fukutsuka, K. Miyazaki, Y. Abe, N. Yoshizawa, T. Abe, Lithium-ion intercalation and deintercalation behaviors of graphitized carbon nanospheres, J. Mater. Chem. A. 6 (2018) 1128–1137, https://doi.org/10.1039/C7TA07902H.

[49] A.P. Cohn, L. Oakes, R. Carter, S. Chatterjee, A.S. Westover, K. Share, C.L. Pint, Assessing the improved performance of freestanding{,} flexible graphene and carbon nanotube hybrid foams for lithium ion battery anodes, Nanoscale 6 (2014) 4669–4675, https://doi.org/10.1039/C4NR00390J.

[50] R. Hu, W. Sun, Y. Chen, M. Zeng, M. Zhu, Silicon/graphene based nanocomposite anode: large-scale production and stable high capacity for lithium ion batteries, J. Mater. Chem. A 2 (2014) 9118–9125, https://doi.org/10.1039/C4TA01013B.

[51] T. Wang, G. Xie, J. Zhu, B. Lu, Elastic reduced graphene oxide nanosheets embedded in germanium nanofiber matrix as anode material for high-performance Li-Ion battery, Electrochim. Acta 186 (2015) 64–70, https://doi.org/10.1016/j.electacta.2015.09.129.

[52] Z. Zeng, V. Murugesan, K.S. Han, X. Jiang, Y. Cao, L. Xiao, X. Ai, H. Yang, J. G. Zhang, M.L. Sushko, J. Liu, Non-flammable electrolytes with high salt-to-solvent ratios for Li-ion and Li-metal batteries, Nat. Energy 3 (2018) 674–681, https://doi.org/10.1038/s41560-018-0196-y.

[53] B. Xu, S. Yue, Z. Sui, X. Zhang, S. Hou, G. Cao, Y. Yang, What is the choice for supercapacitors: graphene or graphene oxide? Energy Environ. Sci. 4 (2011) 2826–2830, https://doi.org/10.1039/C1EE01198G.

[54] J.G. Ren, Q.H. Wu, H. Tang, G. Hong, W. Zhang, S.T. Lee, Germanium-graphene composite anode for high-energy lithium batteries with long cycle life, J. Mater. Chem. A. 1 (2013) 1821–1826, https://doi.org/10.1039/c2ta01286c.

[55] S. Yan, H. Song, S. Lin, H. Wu, Y. Shi, J. Yao, GeO 2 encapsulated Ge nanostructure with enhanced lithium-storage properties, Adv. Funct. Mater. 29 (2019), 1807946, https://doi.org/10.1002/adfm.201807946.

[56] K. Mishra, X.C. Liu, F.S. Ke, X.D. Zhou, Porous germanium enabled high areal capacity anode for lithium-ion batteries, Compos. Part B Eng. 163 (2019) 158–164, https://doi.org/10.1016/j.compositesb.2018.10.076.

[57] K.H. Seng, M.H. Park, Z.P. Guo, H.K. Liu, J. Cho, Catalytic role of ge in highly reversible GeO2/Ge/C nanocomposite anode material for lithium batteries, Nano Lett. 13 (2013) 1230–1236, https://doi.org/10.1021/nl304716e.

[58] P.C.-J. Lee Jae-Young Ngo Duc Tung, Ge–Al multilayer thin film as an anode for Li-ion batteries, J. Korean Ceram. Soc. 54 (2017) 249–256, https://doi.org/10.4191/kcers.2017.54.3.11.

[59] S.-W. Kim, D. Ngo, J. Heo, C. Park, C.-J. Park, Electrodeposited Germanium/Carbon Composite as an Anode Material for Lithium Ion Batteries, Electrochim. Acta 238 (2017), https://doi.org/10.1016/j.electacta.2017.04.027.

[60] C. Zhang, Z. Lin, Z. Yang, D. Xiao, P. Hu, H. Xu, Y. Duan, S. Pang, L. Gu, G. Cui, Hierarchically designed germanium microcubes with high initial coulombic efficiency toward highly reversible lithium storage, Chem. Mater. 27 (2015) 2189–2194, https://doi.org/10.1021/acs.chemmater.5b00218.

[61] P. Lian, X. Zhu, S. Liang, Z. Li, W. Yang, H. Wang, Large reversible capacity of high quality graphene sheets as an anode material for lithium-ion batteries, Electrochim. Acta 55 (2010) 3909–3914, https://doi.org/10.1016/j.electacta.2010.02.025.

[62] D. Yan, X. Xu, T. Lu, B. Hu, D.H.C. Chua, L. Pan, Reduced graphene oxide/carbon nanotubes sponge: a new high capacity and long life anode material for sodium-ion batteries, J. Power Sources 316 (2016) 132–138, https://doi.org/10.1016/j.jpowsour.2016.03.050.

[63] H.F. Xiang, Z.D. Li, K. Xie, J.Z. Jiang, J.J. Chen, P.C. Lian, J.S. Wu, Y. Yu, H. H. Wang, Graphene sheets as anode materials for Li-ion batteries: preparation{,} structure{,} electrochemical properties and mechanism for lithium storage, RSC Adv. 2 (2012) 6792–6799, https://doi.org/10.1039/C2RA20549A.

[64] J. Jo, S. Lee, J. Gim, J. Song, S. Kim, V. Mathew, M.H. Alfaruqi, S. Kim, J. Lim, J. Kim, Facile synthesis of reduced graphene oxide by modified Hummer's method as anode material for Li-, Na- And K-ion secondary batteries, R. Soc. Open Sci. 6 (2019), https://doi.org/10.1098/rsos.181978.

[65] U. Farooq, F. Ahmed, S.A. Pervez, S. Rehman, M.A. Pope, M. Fichtner, E.P. L. Roberts, A stable TiO2-graphene nanocomposite anode with high rate capability for lithium-ion batteries, RSC Adv. 10 (2020) 29975–29982, https://doi.org/10.1039/d0ra05300g.

[66] Z. Yan, J. Guo, High-performance silicon-carbon anode material via aerosol spray drying and magnesiothermic reduction, Nano Energy 63 (2019), 103845, https://doi.org/10.1016/j.nanoen.2019.06.041.

[67] S.W. Kim, D.T. Ngo, J. Heo, C.N. Park, C.J. Park, Electrodeposited germanium/carbon composite as an anode material for lithium ion batteries, Electrochim. Acta 238 (2017) 319–329, https://doi.org/10.1016/j.electacta.2017.04.027.

[68] C. Yue, Z. Liu, W.J. Chang, W. Il Park, T. Song, Hollow C nanobox: an efficient ge anode supporting structure applied to high-performance Li ion batteries, Electrochim. Acta 290 (2018) 236–243, https://doi.org/10.1016/j.electacta.2018.09.075.

[69] Y. Zhang, W. Weng, J. Yang, Y. Liang, L. Yang, X. Luo, W. Zuo, M. Zhu, Lithium-ion battery fiber constructed by diverse-dimensional carbon nanomaterials, J. Mater. Sci. 54 (2019) 582–591, https://doi.org/10.1007/s10853-018-2813-3.

[70] D. Xiong, X. Li, H. Shan, Y. Zhao, L. Dong, H. Xu, X. Zhang, D. Li, X. Sun, Oxygen-containing functional groups enhancing electrochemical performance of porous reduced graphene oxide cathode in lithium ion batteries, Electrochim. Acta 174 (2015) 762–769, https://doi.org/10.1016/j.electacta.2015.06.041.

[71] Y. Xu, X. Zhu, X. Zhou, X. Liu, Y. Liu, Z. Dai, J. Bao, Ge nanoparticles encapsulated in nitrogen-doped reduced graphene oxide as an advanced anode material for lithium-ion batteries, J. Phys. Chem. C 118 (2014) 28502–28508, https://doi.org/10.1021/jp509783h.

[72] B. Wang, Z. Wen, J. Jin, X. Hong, S. Zhang, K. Rui, A novel strategy to prepare Ge@C/rGO hybrids as high-rate anode materials for lithium ion batteries, J. Power Sources 342 (2017) 521–528, https://doi.org/10.1016/j.jpowsour.2016.12.091.

[73] L.C. Loaiza, L. Monconduit, V. Seznec, Si and Ge-based anode materials for Li-, Na-, and K-Ion batteries: a perspective from structure to electrochemical mechanism, Small 16 (2020), 1905260, https://doi.org/10.1002/smll.201905260.

[74] V. Panayotov, M. Panayotova, S. Chukharev, Recent studies on germanium-nanomaterials for LIBs anodes, E3S Web Conf. 166 (2020) 06012, https://doi.org/10.1051/e3sconf/202016606012.

[75] J. Xu, R.D. Deshpande, J. Pan, Y.-T. Cheng, V.S. Battaglia, Electrode side reactions, capacity loss and mechanical degradation in lithium-ion batteries, J. Electrochem. Soc. 162 (2015) A2026–A2035, https://doi.org/10.1149/2.0291510jes.

[76] T. Ungár, J. Gubicza, G. Ribárik, C. Pantea, T.W. Zerda, Microstructure of carbon blacks determined by X-ray diffraction profile analysis, Carbon N. Y 40 (2002) 929–937, https://doi.org/10.1016/S0008-6223(01)00224-X.

[77] G. Krishnamurthy, R. Namitha, Synthesis of structurally novel carbon micro/nanospheres by low temperature-hydrothermal process, J. Chil. Chem. Soc. 58 (2013) 1930–1933, https://doi.org/10.4067/S0717-97072013000300030.

[78] K. Jurkiewicz, M. Pawlyta, A. Burian, Structure of carbon materials explored by local transmission electron microscopy and global powder diffraction probes, C. 4 68 (2018), https://doi.org/10.3390/c4040068.

[79] K. Tasaki, A. Goldberg, J.-J. Lian, M. Walker, A. Timmons, S.J. Harris, Solubility of Lithium Salts Formed on the Lithium-Ion Battery Negative Electrode Surface in Organic Solvents, (2009). https://doi.org/10.1149/1.3239850.

[80] L.Y. Lim, N. Liu, Y. Cui, M.F. Toney, Understanding phase transformation in crystalline Ge anodes for Li-Ion batteries, Chem. Mater. 26 (2014) 3739–3746, https://doi.org/10.1021/cm501233k.

[81] A. Wang, S. Kadam, H. Li, S. Shi, Y. Qi, Review on modeling of the anode solid electrolyte interphase (SEI) for lithium-ion batteries, Npj Comput. Mater. 4 (2018) 15, https://doi.org/10.1038/s41524-018-0064-0.

[82] J. Miao, B. Wang, C.V. Thompson, Kinetic study of lithiation-induced phase transitions in amorphous germanium thin films, J. Electrochem. Soc. 167 (2020), 090557, https://doi.org/10.1149/1945-7111/ab9eec.

[83] A. Lahiri, N. Borisenko, A. Borodin, M. Olschewski, F. Endres, Characterisation of the solid electrolyte interface during lithiation/delithiation of germanium in an ionic liquid, Phys. Chem. Chem. Phys. 18 (2016) 5630–5637, https://doi.org/10.1039/c5cp06184a.

[84] A. Lahiri, G. Li, M. Olschewski, F. Endres, Influence of polar organic solvents in an ionic liquid containing lithium bis(fluorosulfonyl)amide: effect on the cation-anion interaction, lithium ion battery performance, and solid electrolyte interphase, ACS Appl. Mater. Interfaces 8 (2016) 34143–34150, https://doi.org/10.1021/acsami.6b12751.

[85] M. Liu, X. Ma, L. Gan, Z. Xu, D. Zhu, L. Chen, A facile synthesis of a novel mesoporous Ge@C sphere anode with stable and high capacity for lithium ion batteries, J. Mater. Chem. A. 2 (2014) 17107–17114, https://doi.org/10.1039/c4ta02888k.

[86] Q. Li, Z. Zhang, S. Dong, C. Li, X. Ge, Z. Li, J. Ma, L. Yin, Ge nanoparticles encapsulated in interconnected hollow carbon boxes as anodes for sodium ion and lithium ion batteries with enhanced electrochemical performance, Part. Part. Syst. Charact. 34 (2017), 1600115, https://doi.org/10.1002/ppsc.201600115.

[87] Q. Ma, W. Wang, P. Zeng, Z. Fang, Amorphous Ge/C composite sponges: synthesis and application in a high-rate anode for lithium ion batteries, Langmuir 33 (2017) 2141–2147, https://doi.org/10.1021/acs.langmuir.6b04444.

[88] D.T. Ngo, R.S. Kalubarme, H.T.T. Le, J.G. Fisher, C.-N. Park, I.-D. Kim, C.-J. Park, Carbon-interconnected ge nanocrystals as an anode with ultra-long-term cyclability for lithium ion batteries, Adv. Funct. Mater. 24 (2014) 5291–5298, https://doi.org/10.1002/adfm.201400888.

[89] B.L. Oliva-Chatelain, A.R. Barron, Experiments towards size and dopant control of germanium quantum dots for solar applications, AIMS, Mater. Sci. 3 (2016) 1–21, https://doi.org/10.3934/matersci.2016.1.1.

[90] J. Wu, N. Luo, S. Huang, W. Yang, M. Wei, Reversible conversion reaction of GeO2 boosts lithium-ion storage: Via Fe doping, J. Mater. Chem. A. 7 (2019) 4574–4580, https://doi.org/10.1039/c8ta12434e.

[91] S. Leroy, H. Martinez, R. Dedryvère, D. Lemordant, D. Gonbeau, Influence of the lithium salt nature over the surface film formation on a graphite electrode in Li-ion batteries: an XPS study, Appl. Surf. Sci. 253 (2007) 4895–4905, https://doi.org/10.1016/j.apsusc.2006.10.071.

[92] J. Lu, K. Amine, Recent research progress on non-aqueous lithium-air batteries from Argonne National Laboratory, Energies 6 (2013) 6016–6044, https://doi.org/10.3390/en6116016.

[93] K.N. Wood, G. Teeter, XPS on Li-battery-related compounds: analysis of inorganic sei phases and a methodology for charge correction, ACS Appl. Energy Mater. 1 (2018) 4493–4504, https://doi.org/10.1021/acsaem.8b00406.

[94] S. Oswald, F. Thoss, M. Zier, M. Hoffmann, T. Jaumann, M. Herklotz, K. Nikolowski, F. Scheiba, M. Kohl, L. Giebeler, D. Mikhailova, H. Ehrenberg, Binding energy referencing for xps in alkali metal-based battery materials research (II): application to complex composite electrodes, Batteries 4 (2018) 36, https://doi.org/10.3390/batteries4030036.

[95] P. Viswanath, M. Yoshimura, Light-induced reversible phase transition in polyvinylidene fluoride-based nanocomposites, SN Appl. Sci. 1 (2019) 1–9, https://doi.org/10.1007/s42452-019-1564-3.

[96] D. Mandal, K.J. Kim, J.S. Lee, Simple synthesis of palladium nanoparticles, β-phase formation, and the control of chain and dipole orientations in palladium-doped poly(vinylidene fluoride) thin films, Langmuir 28 (2012) 10310–10317, https://doi.org/10.1021/la300983x.

[97] Y. Li, Y. An, Y. Tian, H. Fei, S. Xiong, Y. Qian, J. Feng, Stable and safe lithium metal batteries with Ni-Rich cathodes enabled by a high efficiency flame retardant additive, J. Electrochem. Soc. 166 (2019) A2736–A2740, https://doi.org/10.1149/2.0081913jes.

[98] A.M. Andersson, D.P. Abraham, R. Haasch, S. MacLaren, J. Liu, K. Amine, Surface characterization of electrodes from high power lithium-ion batteries, J. Electrochem. Soc. 149 (2002) A1358, https://doi.org/10.1149/1.1505636.

[99] B. Zhang, L. Li, Z. Wang, S. Xie, Y. Zhang, Y. Shen, M. Yu, B. Deng, Q. Huang, C. Fan, J. Li, Radiation induced reduction: an effective and clean route to synthesize functionalized graphene, J. Mater. Chem. 22 (2012) 7775–7781, https://doi.org/10.1039/c2jm16722k.

[100] J. Zhang, Y. Xu, Z. Liu, W. Yang, J. Liu, A highly conductive porous graphene electrode prepared via in situ reduction of graphene oxide using Cu nanoparticles for the fabrication of high performance supercapacitors, RSC Adv. 5 (2015) 54275–54282, https://doi.org/10.1039/c5ra07857a.

[101] V. Sharova, A. Moretti, T. Diemant, A. Varzi, R.J. Behm, S. Passerini, Comparative study of imide-based Li salts as electrolyte additives for Li-ion batteries, J. Power Sources 375 (2018) 43–52, https://doi.org/10.1016/j.jpowsour.2017.11.045.

[102] Y. Diao, K. Xie, S. Xiong, X. Hong, Insights into Li-S cathode capacity fading mechanisms: irreversible oxidation of active mass during cycling, J. Electrochem. Soc. 159 (2012) A1816–A1821, https://doi.org/10.1149/2.020211jes.

[103] M. Pumera, H. Iwai, Y. Miyahara, Germanium-oxide-coated carbon nanotubes, Nanotechnology 20 (2009), 425606, https://doi.org/10.1088/0957-4484/20/42/425606.

[104] S. Jiao, X. Ren, R. Cao, M. Engelhard, Y. Liu, D. Hu, D. Mei, J. Zheng, W. Zhao, Q. Li, N. Liu, B. Adams, C. Ma, J. Liu, J.-G. Zhang, W. Xu, Stable cycling of high-voltage lithium metal batteries in ether electrolytes, Nat. Energy 3 (2018), https://doi.org/10.1038/s41560-018-0199-8.

[105] K.P.C. Yao, D.G. Kwabi, R.A. Quinlan, A.N. Mansour, A. Grimaud, Y.-L. Lee, Y.-C. Lu, Y. Shao-Horn, Thermal stability of Li2O2 and Li2O for Li-air batteries: in Situ XRD and XPS studies, J. Electrochem. Soc. 160 (2013) A824–A831, https://doi.org/10.1149/2.069306jes.